SCALING EFFECT ON BUBBLE DYNAMICS IN A TIP VORTEX FLOW: PREDICTION OF CAVITATION INCEPTION AND NOISE

by

Chao-Tsung Hsiao[1], Georges L. Chahine[1], and Han-Lieh Liu[2]

November 2000

info@dynaflow-inc.com

http://www.dynaflow-inc.com

This work was conducted in partial fulfillment of Contract No. N00174-96-C-0034 for the Naval Surface Warfare Center, Indian Head Division, Technical Monitor: Gregory Harris, Harrisgs@ih.navy.mil

[1] DYNAFLOW, INC. 7210 PINDELL School Road, Fulton MD 20759

[2] Naval Surface Warfare Center, Carderock Division, Bethesda, MD 20084-5000, liuhl@nswccd.navy.mil

TABLE OF CONTENT

LIST OF FIGURES

LIST OF TABLES

ABSTRACT

This report considers the prediction of tip vortex cavitation inception at a fundamental physics based level. Starting form the presumption that cavitation inception detection is based on the "monitoring" of the interaction between bubble nuclei present in the water and the flow field of the propeller blade, the bubble dynamics is investigated in detail. Spherical and 3D bubble dynamics models are implemented and used to study numerically the dynamics of a nucleus in an imposed flow field. The codes provide bubble size, position, and shape variations versus time as well as the resulting pressure at any selected monitoring position.

In the report we exercise extensively the spherical model, which has the merit of allowing long time simulations, and to a lesser extent, the non-spherical codes. Non-spherical deformations are very important when large pressure gradients exist at the bubble location. When this occurs, the simulations show that strong bubble deformation leading to re-entering jet formation and bubble splitting may occur even while the bubble is growing during its capture by the vortex. These dynamic phenomena may cause high frequency acoustic emission due to the collision and separation of air/liquid interfaces. This also makes long time numerical computations difficult without significant additional numerical development.

The spherical model is used to conduct a parametric study, and the results are presented. Bubble size and emitted sound variations versus time are presented for various nuclei sizes and flow field scales in the case of an ideal Rankine vortex to which a longitudinal viscous core size diffusion model is imposed. Based on the results, one can deduce cavitation inception with the help of either an *"optical inception criterion"* (maximum bubble size larger than a given value) or an *"acoustical inception criterion"* (maximum detected noise higher than a given background value). We use here such criteria and conclude that scaling effects can be inherent to the way in which these criteria are exercised if the bubble dynamics knowledge is not taken into account. The use of the procedures developed leads to a wealth of information that a cavitation researcher can use to draw needed conclusions for his study. We have used it, for instance here, to obtain cavitation inception criteria at various scales and to attempt to deduce scaling laws for the amplitude and frequency of bubble generated acoustic noise, and in a parallel study to deduce scaling laws for maximum bubble radius and frequency.

ACKNOWLEDGEMENTS

This work was conducted at DYNAFLOW in execution of a Task Order under the contract **N00174-96-C-0034** with the Naval Surface Warfare Center Indian Head Division. Funding was provided by the Naval Surface Warfare Center Carderock Division, from the Propulsor Group, Mr. Jude Brown. Dr. Han Lieh Liu from NSWCCD was the driving force behind the project and made many suggestions and contributions to the project. At DYNAFLOW we benefited from comments and discussions by many colleagues that we would like to thank here. More particularly, Damien Puygrenier who was a summer student from Ecole Centrale de Lyon helped with the latest version of the developed code. Dr. Young Shen from NSWCCD, contributed by his insightful questions and comments while monitoring a project complementary to the one described in this report. We would like to thank these various colleagues for their support and significant contributions to this study.

1. INTRODUCTION

It is common to predict tip vortex cavitation inception using small-scale laboratory setting. The challenge is then to find the correct scaling laws to extrapolate the results to the full scale. While the present knowledge enables engineers to proceed properly with this scaling in many cases, there are conditions where classical scaling as defined below needs to be reconsidered and corrected. This report aims at contributing to our knowledge to provide such a more general scaling.

In practice, engineering prediction of cavitation inception is made by equating the cavitation inception number to the negative of the minimum pressure coefficient neglecting real flow effects such as flow viscosity and unsteadiness, water quality, nuclei dynamics and bubble/flow interactions. These ignored effects sometimes lead to significant discrepancies between model and full-scale tests due to what is known as the "*scale effects*".

The cavitation number, σ, which is the non-dimensional parameter used to characterize overall cavitation effects is defined as:

$$\sigma = \frac{p_\infty - p_v}{1/2\rho V_\infty^2}, \tag{1.1}$$

where p_∞ and V_∞ are the characteristic pressure and velocity (usually at free stream), ρ is the liquid density, and p_v is the liquid vapor pressure. Following McCormick (1962), several experimental studies (DTRC, Fruman et al. 1991, Arndt et al. 1992, Maines and Arndt 1993) have established the following scaling law to predict steady tip vortex cavitation inception for finite-span hydrofoils:

$$\sigma_i = KC_l^2 \, \mathrm{R_e}^{0.4}, \quad \text{with} \quad \mathrm{R_e} = \frac{V_\infty C_0}{\upsilon}. \tag{1.2}$$

Equation (1.2) correlates the cavitation inception number, σ_i, to the boundary layer growth in the tip region. C_l is the foil lift coefficient, Re is the flow Reynolds number and K is a proportionality constant, which depends on the foil geometry and the flow incidence. However, it is well known that the inception of tip vortex cavitation is very sensitive to the nuclei size and number in the flow. Arndt and Keller (1992) introduced a correction term to Equation (1.2) based on the tensile strength of the liquid to account for the water quality because the onset of cavitation in "*weak*" water (very small tensile strength) and "*strong*" water (large tensile strength) is quite different. However, the effect of nuclei size distribution in the liquid *per se* was not directly accounted for in that study.

Direct experimental observation of bubble capture by the tip vortex is difficult due to the small size of the nuclei and the high local velocities. This usually lead to the ignorance of where the bubble is captured. Numerical studies, therefore, have been used primarily to study the dynamics of nuclei. The complexity of the cavitation inception process, however, has led various numerical studies to neglect one or more of the factors, and therefore to only investigate the influence of a limited set of parameters. Since tip vortex cavitation inception is usually considered to be a traveling bubble form of cavitation, a spherical bubble dynamics model coupled with a motion equation has been frequently applied to predict the cavitation inception in a tip vortex. Latorre (1982) and Ligneul and Latorre (1989) applied this approach to deduce noise emission from cavitation in a Rankine line vortex. Hsiao and Pauley (1999) further applied this approach to study tip vortex cavitation inception with the tip vortex flow field computed by Reynolds-Averaged Navier-Stokes equation. This approach, however, neglected non-spherical bubble deformations and bubble/flow interactions, which may significantly alter the cavitation inception process. Using a three-dimensional non-spherical bubble dynamics model, Chahine (1990, 1995) showed that due to a large pressure gradients the bubble while growing deforms to a non-spherical shape and forms a re-entering jet directed toward the vortex core when approaching the vortex center during its capture. The development of a re-entering jet may result in liquid-liquid impact, bubble splitting, and sound emission before the bubble reaches the vortex axis. Chahine also used an axisymmetric non-spherical model to simulate bubble dynamics for the bubble in the vortex center. Depending on different initial bubble size and ratios of gas to ambient pressure, the bubble surface collapsed in different ways after the bubble elongates. It is hypothesized that bubble surface collapse and splitting, in addition to bubble volume change, would emit high frequency noise and modify the criteria for inception when cavitation inception is determined using acoustic techniques. These predictions were confirmed with high-speed photography of the interaction between a bubble and a vortex ring (Chahine et al, 1993) and very recently by Gopalan et al (2000) and Arndt and Maines (2000).

The current study makes a concerted effort to investigate the importance of the various factors influencing tip vortex cavitation inception. The tip vortex flow generated by a three-dimensional foil can be idealized as a simple Rankine line vortex. Conventional empirical equations are used to estimate the vortex strength and core size for three different geometric scales of a foil. To investigate the effect of nuclei size, an improved spherical bubble dynamics model is implemented and is used to predict the cavitation inception. Both the so-called '*acoustic*' criterion (emitted sound level higher than a threshold value) and the '*optical*' criterion (bubble size larger than a threshold value) are considered for determining the cavitation inception. A non-spherical bubble dynamics is then applied to study the importance of non-spherical deformations on the prediction of cavitation inception.

2. CLASSICAL APPROACHES FOR SCALING TIP VORTEX CAVITATION INCEPTION

2.1 General Cavitation Scaling

Classical approaches for predicting the cavitation inception are often made by equating the cavitation inception number at inception to the negative of the minimum pressure coefficient. Since there is no experimental technique presently to measure the pressure inside the vortex core without intrusion, this pressure is usually estimated utilizing the measured circumferential velocity. By assuming an axisymmetric velocity profile near the tip, one can compute the pressure coefficient by:

$$C_p = -2\int_0^{\infty} \frac{V_t^2}{V_\infty^2} \frac{dr}{r} \approx -\left(\frac{V_{t\max}}{V_\infty}\right)^2 , \tag{2.1}$$

where V_∞ is the free stream velocity and $V_{t\max}$ is the maximum circumferential velocity.

McCormick (1962) proposed, for the first time, that the boundary layer developed over the lower surface of the foil near the tip determines the extent of the vortex core. In his semi-empirical approach he postulated a power law relationship between the boundary layer thickness, δ, and the Reynolds number based on V_∞ and the chord length C_0,

$$\delta \simeq \mathrm{R_e}^{-\alpha}. \tag{2.2}$$

Since no detailed velocity measurements in the region near the tip were available at that time, the flow was analyzed by the lifting line theory. As a result, $V_{t\max}$ was obtained by computing the induced downwash velocity at 0.5δ outboard of the foil. This leads to C_p being roughly inversely proportional to δ. He then deduced $\alpha = 0.35$ based on his experimental measurements of critical cavitation inception number.

Later experimental measurements of the velocity near the tip region (Fruman *et al*. 1991, Arndt *et al.* 1991) all confirmed that the tip vortex viscous core has a solid body rotation, and that the local maximum circumferential velocity is almost proportional to the ratio of local vortex circulation, Γ, and vortex core radius, a_c, *i.e.*

$$V_{t\max} \simeq \frac{\Gamma}{a_c}. \tag{2.3}$$

On the basis of these previous studies, it appears that the local vortex circulation and core size are respectively a fraction of the mid-span bound circulation, Γ_0, and boundary layer thickness, δ_0, on the pressure side. From classic thin wing theory (Abbott and Doenhoff 1959) one has

$$\Gamma_0 = \frac{1}{2} C_l C_0 V_\infty . \tag{2.4}$$

The lifting coefficient, C_l, can be determined by

$$C_l = 2\pi (A_0 + \frac{1}{2} A_1) , \tag{2.5}$$

where the coefficient A_0 depends only on the angle of attack and the coefficient A_1 depends only on the shape of the mean line.

The turbulent boundary layer thickness δ on the pressure side can be estimated as for a fully turbulent boundary layer over a flat plate (Schlichting 1979)

$$\delta = 0.37 C_0 \left(\frac{V_\infty C_0}{\nu} \right)^{-0.2} . \tag{2.6}$$

Substituting Equation (2.3), (2.4) and (2.6) into (2.1), the pressure coefficient can then be expressed as:

$$C_p \approx -C_l^{\,2} \left(\frac{V_\infty C_0}{\nu} \right)^{0.4} = -K C_l^{\,2} \, \mathrm{R_e}^{0.4} . \tag{2.7}$$

Several experimental studies (e.g. Fruman *et al.* 1992 and Arndt, *et al.* 1992) have shown a good agreement between incipient cavitation number, σ_i and $-C_{p\min}$ after using Equation (2.7) to estimate the $-C_{p\min}$ in the tip vortex.

2.2 The Rankine Vortex Model

Developments in laser anemometry have allowed several researchers to determine the velocity distribution in a tip vortex flow. While the flow very close to the tip is not exactly symmetric, the tangential velocity profile has two very distinct region: for radial distances less than the "*viscous core*" size, a_c, the tangential velocity varies nearly linearly with the distance to the core center where this velocity is zero. For locations larger than a_c, the tangential velocity decays with distance as the function 1/r. Figure 1 reproduces experimental results taken from

LeGuen (1998) and illustrates the existence of the two regions described above, i.e. a viscous core solid body rotation central region, and an inviscid potential vortex outside region.

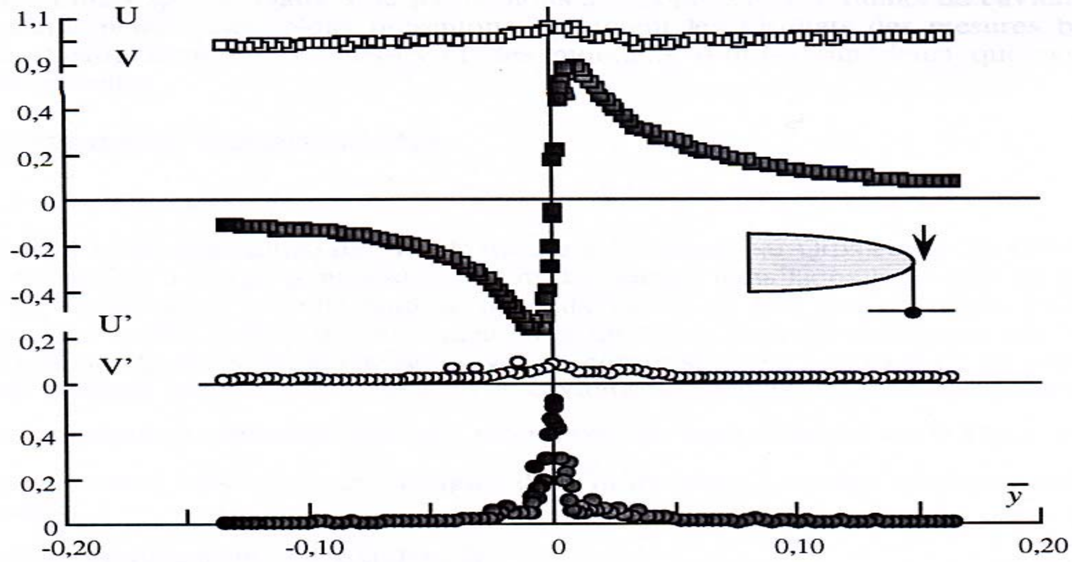

Figure 1. Velocity and fluctuations profiles at a distance of $0.5C_0$ from the tip of an elliptic foil at an incidence of 10º (from LeGuen, 1998).

The Rankine model gives the following expressions for the velocity, V_t, and pressure, p_ω:

$$V_t(r) = \begin{Bmatrix} \dfrac{\Gamma}{2\pi\, a_c{}^2} r, \; r \le a_c \\ \dfrac{\Gamma}{2\pi\, r}, \quad r \ge a_c \end{Bmatrix}, \tag{2.8}$$

$$p_\omega(r) = \begin{Bmatrix} p_\infty - \dfrac{\rho\Gamma^2}{4\pi^2\, a_c{}^2} + \dfrac{\rho\Gamma^2}{8\pi^2\, a_c{}^4} r^2, \; r \le a_c \\ p_\infty - \dfrac{\rho\Gamma^2}{8\pi^2\, r^2}, \quad r \ge a_c \end{Bmatrix}. \tag{2.9}$$

In the present study we consider the tip vortex generated by finite-span hydrofoils and consider three different sizes, small (laboratory 1/48th scale), medium (1/4th scale), and large (full scale). These hydrofoils are geometrically similar and are operated at the same angle of attack.

The circulation strength, Γ, for these three scales is estimated as described in (2.4), and for the particular foils considered here we will use

$$\Gamma = 0.04 * 2\pi C_0 V_\infty , \tag{2.10}$$

The vortex core size, a_c, is estimated by Equation (2.6)

$$a_c = \delta = \frac{0.37 C_0}{\mathrm{R_e}^{0.2}} \tag{2.11}$$

From Equation (2.9), the minimum pressure coefficient in the vortex center is then determined by

$$C_{p\,\mathrm{min}} = -\frac{1}{2\pi^2 V^2}\left(\frac{\Gamma}{a_c}\right)^2 , \tag{2.12}$$

which for the particular foils considered here leads to:

$$C_{p\,\mathrm{min}} = -0.00234\,\mathrm{Re}^{0.4} , \tag{2.13}$$

The flow parameters for these three cases are shown in Table 1.

	Small Scale	**Medium Scale**	**Large Scale**
λ	1/48	1/4	1
C_0 (m)	0.0508	0.6096	2.4384
V_∞ (m/sec)	10	12.5	15
Γ (m^2/sec)	0.12767	1.91511	9.19255
$\mathrm{R_e}$	5.08×10^5	7.62×10^6	3.66×10^7
a_c (m)	0.001358	0.009486	0.02770
$C_{p\,\mathrm{min}}$	-4.474	-13.215	-24.797

Table 1: **Conditions of scaled tests simulated**

3. NUMERICAL METHODS

3.1 Spherical Model

3.1.1 Improved Spherical Bubble Dynamics Model

The behavior of a spherical bubble in a pressure field is usually described with a relatively simple bubble dynamics model known as the Rayleigh-Plesset equation (Plesset 1948)

$$R\ddot{R}+\frac{3}{2}\dot{R}^2=\frac{1}{\rho}\left(p_v+p_g-p-\frac{2\gamma}{R}-\frac{4\mu}{R}\dot{R}\right), \tag{3.1}$$

where R is the time dependent bubble radius, ρ is the liquid density, p_v is the vapor pressure, p_g is the gas pressure inside the bubble, p is the ambient pressure local to the bubble, μ is the liquid viscosity, γ is the surface tension. If the gas is assumed to be perfect and to follow a polytropic compression relation, then one has the following relationship between the gas pressure and the bubble radius:

$$p_g=p_{g0}\left(\frac{R_0}{R}\right)^{3k}, \tag{3.2}$$

where p_{g0} and R_0 are the initial gas pressure and bubble radius respectively and k is the polytropic gas constant. In Equation (3.1) the bubble grows principally in response to a change in the ambient pressure through gaseous expansion and increase in the vaporous mass within the bubble (the vapor pressure is assumed to remain constant). In this modeling the effect of the underlying flow is only to produce a prescribed pressure field through which the bubble is passively convected, i.e. the influence of the bubble on the liquid flow is neglected.

In addition, Equation (3.1) does not take into account the effect of any slip velocity between the bubble and the carrying liquid. To account for this slip velocity, an additional pressure term, $\rho(\vec{U}-\vec{U}_b)^2/4$, is added to the classical Rayleigh-Plesset equation as (see Appendix for detailed derivation):

$$R\ddot{R}+\frac{3}{2}\dot{R}^2=\frac{1}{\rho}\left[p_v+p_{g0}\left(\frac{R_0}{R}\right)^{3k}-p-\frac{2\gamma}{R}-\frac{4\mu}{R}\dot{R}\right]+\frac{\left(\vec{U}-\vec{U}_b\right)^2}{4}. \tag{3.3}$$

The above equations (3.1, 3.3) are valid when the liquid is incompressible. However, liquid compressibility becomes important when bubble-wall velocities become comparable with the speed of sound in the liquid. Compressibility effects are also important if one is interested in many cycles of the bubble dynamics in which case energy loss by acoustic emission occurs. An efficient modification of the Rayleigh-Plesset equation that takes into account liquid compressibility was obtained by Gilmore (1952). We adapt Gilmore's equation and write the modified Rayleigh-Plesset equation as:

$$(1-\frac{\dot{R}}{c})R\ddot{R}+\frac{3}{2}(1-\frac{\dot{R}}{3c})\dot{R}=\frac{1}{\rho}(1+\frac{\dot{R}}{c}+\frac{R}{c}\frac{d}{dt})\left[p_v+p_{g0}\left(\frac{R_0}{R}\right)^k-p_\infty-\frac{2\gamma}{R}-4\mu\frac{\dot{R}}{R}\right]+\frac{\left(\vec{U}-\vec{U}_b\right)^2}{4},\qquad(3.4)$$

where c is the sound speed.

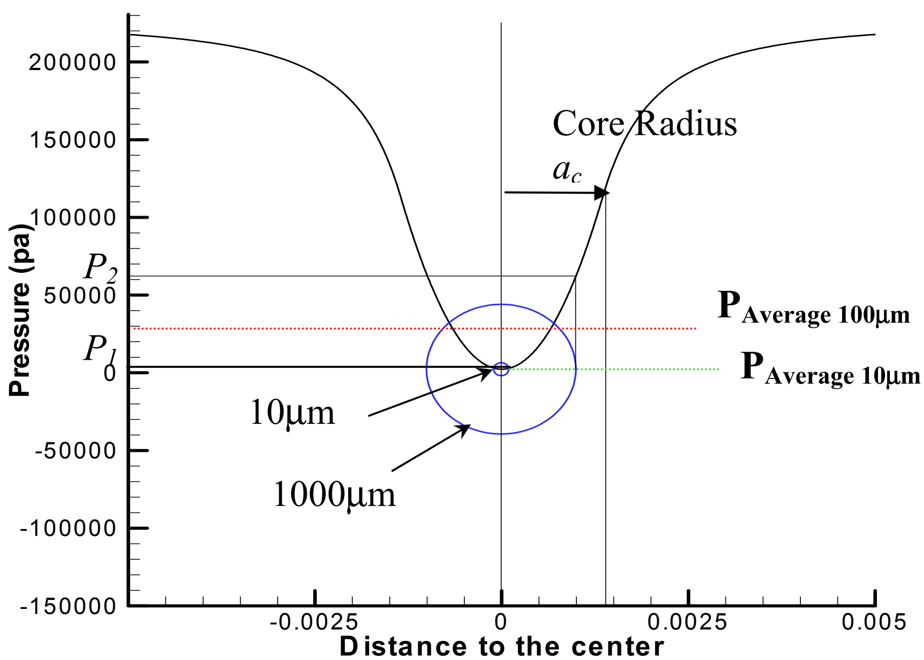

Figure 2. Illustration of the pressure-averaging concept in the core of the vortex. The 100 μm bubble sees a much larger average pressure that the 10 μm bubble.

It is known that the ambient pressure, p, applied in the classical spherical bubble model is the pressure at the bubble center in its absence, without considering pressure variation along the bubble surface. This simplification, valid for general flows, leads to unbounded bubble growth when the pressure in the vortex center is less than the vapor pressure. Previous studies usually used this as a criterion to determine the cavitation inception number. However, this criterion is based on an over-simplification that may lead to wrong predictions. Therefore, *in the improved model* we use here, *p is taken to be the average of the outside field pressure over the bubble surface*. This enables for a much more realistic description of the bubble behavior, e.g. the bubble does not continuously grow as it is captured by the line vortex. Instead, once the bubble reaches the vortex line axis, it is subjected to an increase in the average pressure as the bubble grows and this lead to a more realistic balance of the forces applied to the bubble. Figure 2 illustrates how the pressure to which the bubble is subjected increases as the bubble grows say from a radius of 10μm to a radius of 100μm.

3.1.2 Bubble Motion Equation

The motion equation of a spherical particle subjected to the force of gravity in a fluid at rest has been derived by several prominent scientist such as Basset (1888), Boussinesq (1903), Oseen (1927). The equation was extended by Tchen (1947) to the case of a fluid moving with variable velocity and more recently modified by Maxey and Riley (1983). By considering the forces acting on a spherical bubble with radius R the motion equation can be written as follows:

$$\begin{aligned}\rho_b V_b \frac{d\vec{U}_b}{dt} &= V_b(\rho_b-\rho)\vec{g} + V_b\nabla p + \frac{1}{2}\rho A_b C_D\left(\vec{U}-\vec{U}_b\right)\left|\vec{U}-\vec{U}_b\right| \\ &+\frac{1}{2}\rho V_b\left(\frac{d\vec{U}}{dt}-\frac{d\vec{U}_b}{dt}\right)+6A_b\sqrt{\frac{\rho\mu}{\pi}}\int_0^t\left(\frac{d\vec{U}}{d\tau}-\frac{d\vec{U}_b}{d\tau}\right)\Big/\sqrt{t-\tau}\,d\tau\end{aligned}, \tag{3.5}$$

where terms with the subscript b are related to the bubble and those without a subscript are related to carrying fluid. V_b and A_b are the bubble volume and projected area, which are equal to $4/3\pi R^3$ and πR^2 respectively. The bubble drag coefficient C_D in Equation (3.5) can be determined by using the empirical equation of Haberman and Morton (1953):

$$C_D = \frac{24}{\mathrm{R}_{\mathrm{e}\,b}}\left(1+0.197\,\mathrm{R}_{\mathrm{e}b}^{0.63}+2.6\times10^{-4}\,\mathrm{R}_{\mathrm{e}b}^{1.38}\right), \tag{3.6}$$

where the bubble Reynolds number is defined as

$$\mathrm{R}_{\mathrm{e}b} = \frac{2R\left|\vec{U}-\vec{U}_b\right|}{\nu}. \tag{3.7}$$

The physical meaning of each term in the right hand side of Equation (3.5) is as follows. The first term is a buoyancy force. The second term is due to the pressure gradient in the fluid surrounding the particle. The third term is a drag force. The fourth term is a force to accelerate the virtual "added mass" corresponding to the surrounding fluid. The last term is the so-called "Basset" term, which is a memory effect term, which takes into account the deviation of the flow pattern from steady state. Equation (3.5), however, does not include the lift force, which is caused by the particle spin.

An analysis by Morrison and Stewart (1976) shows that the "Basset" term depends on the rate of change of the relative velocity. For flows in which the frequency of the oscillatory motion of the carrier fluid is small the Basset term can be neglected. Furthermore, Maxey and Riley (1983) have presented order of magnitude estimates for various forces acting in the bubble. They concluded that once the motion is established, the Basset history term is only of a secondary order when compared to other forces. Since in this study, we release the bubble with the same initial velocity as its surrounding liquid, we will neglect the "Basset" term.

Equation (3.5) describes the motion of a solid particle in a flow. For a gas bubble the mass of the gas inside the bubble can be neglected relative to the added mass of the fluid. To describe the motion of a gas bubble, however, one has to take into account the force due to the bubble volume variation. Johnson and Hsieh (1966) added the term necessary to consider the bubble volume variations as follows:

$$\frac{d\vec{U}_b}{dt} = -2\vec{g} + \frac{3}{\rho}\nabla p + \frac{3}{4}C_D\left(\vec{U}-\vec{U}_b\right)\,\left|\,\vec{U}-\vec{U}_b\right| + \frac{3}{R}\left(\vec{U}-\vec{U}_b\right)\dot{R}\,. \qquad (3.8)$$

With a prescribed flow field, a Runge-Kutta fourth-order scheme can be applied to integrate Equations (3.8) and (3.3) or (3.4) through time to provide the bubble trajectory and its volume variation during bubble capture by the tip vortex.

The pressure in the liquid at a distance, *l*, from the bubble center is given by:

$$p = \frac{\rho}{l}\left[R^2\ddot{R} + 2R\dot{R}^2\right] \text{-}\rho\left[\frac{R^4\dot{R}^2}{2l^4}\right]. \qquad (3.9)$$

Far away from the bubble the second bracketed term is negligible, and Equation (3.9) degenerates to the equation usually given to the acoustic pressure for instance by Fitzpatrick and Strasberg (1958):

$$p_a(t') = \frac{\rho\ddot{V}(t')}{4\pi l}, \qquad t' = t - \frac{l-R}{c}\,. \qquad (3.10)$$

Since the bubble volume is V=4/3πR^3 we have

$$p_a(t') = \frac{R\rho}{l}\left[R\ddot{R}(t') + 2\dot{R}^2(t')\right] \ , \tag{3.11}$$

where p_a is the acoustic pressure and c is the sound speed.

3.2 Non-Spherical Bubble Dynamics Model

To study bubble dynamics during bubble capture by a vortex and non-spherical bubble deformation, a non-spherical bubble dynamics model based on the Boundary Element Method (BEM) is applied. This model assumes that the flow due to the bubble presence is potential and that the vortical flow describing the vortex is not modified by the bubble presence and dynamics.

This model is developed using the fact that any velocity field u can be expressed via the Helmholtz decomposition as the sum of the gradient of a scalar potential ϕ and the curl of a vector potential A (Chahine et al. 1997):

$$\begin{aligned} &\mathrm{u} = \mathrm{u}_p + \mathrm{u}_\omega = \nabla\phi + \nabla\times\mathrm{A}. \\ &\nabla^2\phi = 0; \qquad \nabla^2 A = -\varpi. \end{aligned} \tag{3.12}$$

Since ϕ satisfies the Laplace equation, one can apply Green's identity to express ϕ as:

$$\Omega\phi = \int_S [\phi(\mathrm{x}')\frac{\partial G}{\partial n}(\mathrm{x},\mathrm{x}') - \frac{\partial\phi}{\partial n}(\mathrm{x}')G(\mathrm{x},\mathrm{x}')] \ \ dS(\mathrm{x}'), \tag{3.13}$$

where Ω is the solid angle subtended by the fluid at the point x and $G(\mathrm{x},\mathrm{x}') = -|\,\mathrm{x}-\mathrm{x}'\,|^{-1}$ is the free space Green's function. To solve Equation (3.13) with the BEM, we discretize the bubble surface by triangular elements and then rewrite the equation in a discretized form as

$$\Omega\phi(x_i) = \sum_{j=1}^{N}\left[A_{ij}(x_i,x_j')\frac{\partial\phi}{\partial n}(x_j') - B_{ij}(x_i,x_j')\phi(x_j')\right]; \qquad i = 1,...,N, \tag{3.14}$$

where A_{ij} and B_{ij} are elements of the influence matrices in (3.13) and N is the number of the discretized nodes on the bubble surface. Equation (3.14) can be applied to determine the normal velocity $\partial\phi/\partial n$ on the bubble surface provided that the velocity potential ϕ over the bubble surface is known. For time stepping procedure, all the nodes on the bubble surface are moved to their new positions using the displacement $\partial\phi/\partial n\cdot\vec{e}_n + V_t\cdot\vec{e}_t$ where $\vec{e}_n$ and $\vec{e}_t$ are the unit normal and tangential vectors at the bubble surface, and V_t is the tangential velocity. At the next time step, ϕ is updated by

$$\phi^{n+1} = \phi^n + \left(\frac{\partial \phi^n}{\partial t} + (\mathrm{u}_p + \mathrm{u}_\omega) \cdot \nabla \phi^n \right) \Delta t. \tag{3.15}$$

To determine $\partial\phi / \partial t$ one needs to start from substituting Helmholtz decomposition into the Navier-Stokes equation:

$$\begin{aligned} \frac{\partial \mathbf{u}_p}{\partial t} + \frac{\partial \mathbf{u}_\omega}{\partial t} - (\mathbf{u}_p + \mathbf{u}_\omega) \times \left[\nabla \times (\mathbf{u}_p + \mathbf{u}_\omega) \right] + \nabla \left(\frac{1}{2} \left| \mathbf{u}_p + \mathbf{u}_\omega \right|^2 \right) \\ = -\frac{\nabla p}{\rho} + \nu \nabla^2 (\mathbf{u}_p + \mathbf{u}_\omega) \ . \end{aligned} \tag{3.16}$$

With the assumption that the vortex flow field is not modified by the presence of the bubble, the vortex flow is predetermined and also satisfies the Navier-Stokes equation:

$$\frac{\partial \mathrm{u}_\omega}{\partial t} - \mathrm{u}_\omega \times (\nabla \times \mathrm{u}_\omega) + \nabla \left(\frac{1}{2} \left| \mathrm{u}_\omega \right|^2 \right) = -\frac{\nabla p_\omega}{\rho} + \nu \nabla^2 \mathrm{u}_\omega. \tag{3.17}$$

Substitute Equation (3.16) to Equation (3.15), one can obtain a modified Bernoulli equation:

$$\nabla \psi = \nabla \left(\frac{\partial \phi}{\partial t} + \frac{1}{2} \left| \nabla \phi \right|^2 + \mathrm{u}_\omega \cdot \nabla \phi + \frac{p - p_\omega}{\rho} \right) = \nabla \phi \times (\nabla \times \mathrm{u}_\omega). \tag{3.18}$$

For the particular case of the Rankine line vortex, we have $\nabla \times \mathrm{u}_\omega = \omega_z \vec{e}_z$. Multiplying Equation (3.18) by $\vec{e}_z$ results in

$$\frac{\partial \psi}{\partial z} = 0. \tag{3.19}$$

Equation (3.19) indicates that ψ is constant along the vortex axial direction. Since $\phi = 0$ at $z = \infty$, we obtain:

$$\frac{\partial \phi}{\partial t} + \frac{1}{2} \left| \nabla \phi \right|^2 + \mathrm{u}_\omega \cdot \nabla \phi + \frac{p - p_\omega}{\rho} = \frac{p(\infty) - p_\omega(\infty)}{\rho} = 0. \tag{3.20}$$

By substituting Equation (3.20) into Equation (3.15), Equation (3.15) can be rewritten as

$$\phi^{n+1} = \phi^n + \left(\frac{1}{2} \left| \nabla \phi \right|^2 + \frac{p - p_\omega}{\rho} \right) \Delta t, \tag{3.21}$$

where p can be obtained from the dynamic boundary condition, *i.e.* normal stress balance on the bubble surface:

$$p = p_g + p_v - C\gamma - 2\mu \frac{\partial^2 \phi}{\partial n^2}, \tag{3.22}$$

where P_g is the gas pressure and C is the local bubble surface curvature.

To determine the pressure generated by the bubble in the field, a second Green's identity is applied to compute $\partial\phi/\partial t$

$$\Omega\frac{\partial}{\partial t}=\int_S[\frac{\partial}{\partial t}(\mathbf{x}')\frac{\partial G}{\partial n}(\mathbf{x},\mathbf{x}')-\frac{\partial^2}{\partial n\partial t}(\mathbf{x}')G(\mathbf{x},\mathbf{x}')]\quad dS(\mathbf{x}'), \tag{3.23}$$

with the acoustic pressure being predominantly $p_a=-\partial\phi/\partial t$.

4. NUMERICAL STUDY

4.1 Cavitation Inception Criteria

Although many different definitions of cavitation inception have been suggested and applied by different researchers, there are practical complications in determining consistently the actual cavitation inception event. The precise notion of cavitation inception as a practically observed phenomenon in contrast to a mathematical consequence of an equation is a matter of discussion. From an engineering viewpoint, cavitation inception is usually determined through visual or acoustical techniques. Inception is called when the measurement detects events above a pre-defined threshold, in which case an additional notion of number of events per unit time above the threshold is required to avoid spurious noise data. In the laboratory the most commonly used threshold is via visual observation when bubbles are seen. This visual technique can hardly be applied to full-scale tests where an acoustic technique is usually preferred. In the acoustic technique, the cavitation inception event can be defined either by the sound amplitude level (absolute noise level or relative value over the background noise) and/or by the appearance of some characteristic frequencies. In the current study, both the acoustic and the optical criteria are investigated for determining the cavitation inception. In the following we will also show the importance of the selection of the bubble dynamics model on the results.

4.2 Scaling of Inception Using the Classical Rayleigh-Plesset Model

To study the scaling effect on the prediction of cavitation inception, first the classical incompressible Rayleigh-Plesset spherical model was applied to predict the cavitation inception number, σ, for the three scales described earlier. Different initial nuclei sizes were also considered to study the effect of the bubble size distribution in the liquid on cavitation inception. The computations were conducted by releasing bubbles far away from the vortex core (D=3a_c where D is the distance between the bubble and the vortex axis) with an initial nucleus equilibrium condition, i.e. the initial gas pressure is:

$$p_{g0} = p_{\omega}(D) - p_v + \frac{2\gamma}{R_0}, \tag{4.1}$$

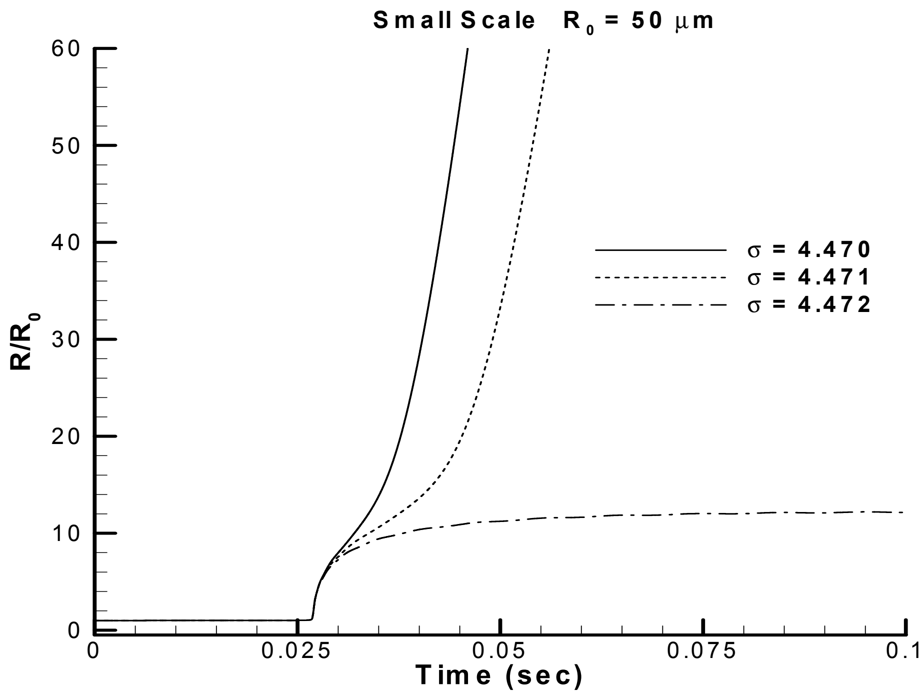

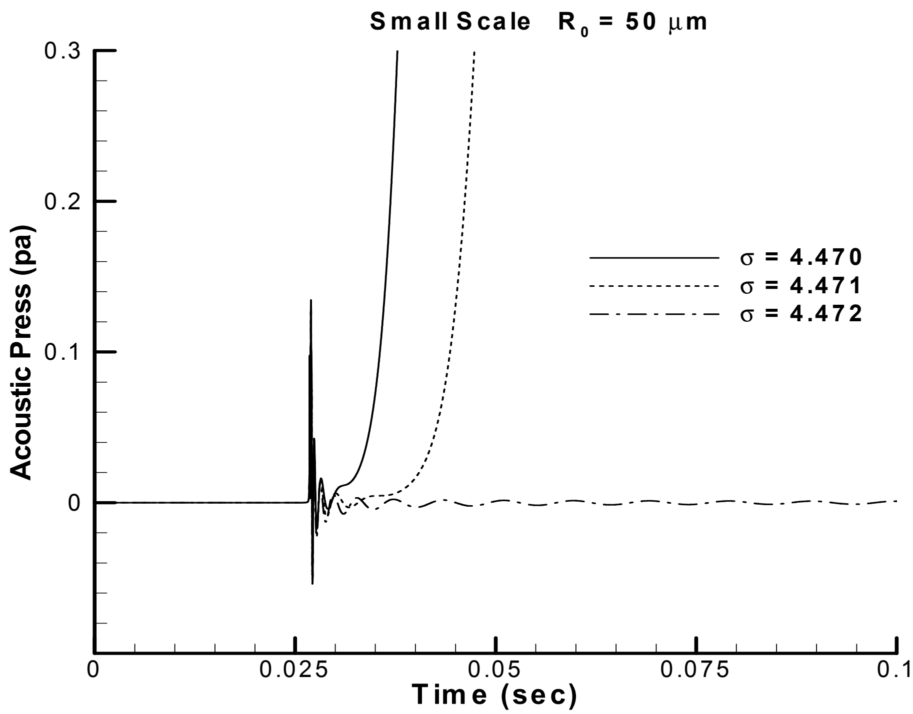

Figure 3. Bubble radius versus time and generated acoustic pressure at a distance of 30 cm. using the classical Rayleigh-Plesset equation.

where $p_\omega(D)$ is computed by Equation (2.8). Figure 3 shows for the small-scale case the bubble radius and the acoustic pressures versus time for three different cavitation numbers close to the condition of unbounded bubble growth. The cavitation inception number for each case, shown in Table 2, was determined as *the highest cavitation number that leads to an unbounded bubble growth*. In the classical explanation, the unbounded bubble growth results in the vaporous cavitation while the limited bubble growth is described as gaseous cavitation. Using this simple model, we found that the predicted cavitation inception numbers for all cases are very close to those predicted by using the simple engineering criterion, $\sigma_i = -Cp_{min}$ and can be scaled by the relationship described earlier in Equation (2.13). The results, shown in Figure 4, obviously do not explain measured scaling effects in the experimental observations.

R_0	Small Scale	Medium Scale	Large Scale
10μm	$\sigma_i = 4.467$	$\sigma_i = 13.212$	$\sigma_i = 24.796$
50 μm	$\sigma_i = 4.471$	$\sigma_i = 13.214$	$\sigma_i = 24.796$
100μm	$\sigma_i = 4.473$	$\sigma_i = 13.214$	$\sigma_i = 24.796$

Table 2. Cavitation inception index using the classical spherical model approach

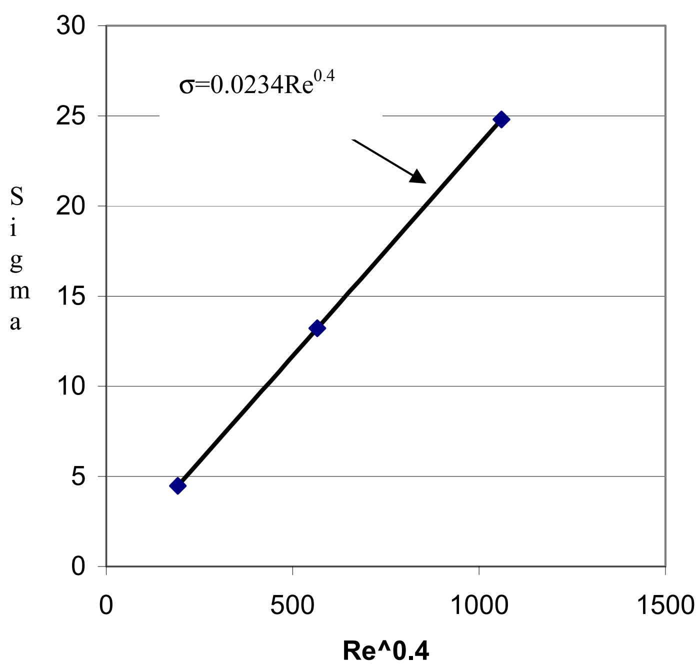

Figure 4. Correlation between cavitation inception indices and the Reynolds number obtained with the classical model and compared with the curves of $-C_{pmin}$

4.3 Scaling of Inception Using the "Modified" Rayleigh-Plesset Model

The cavitation inception results obtained in Table 2 are mainly due to accepting that the bubble can grow unboundedly once it reaches the vortex center. To account for the fact that the average pressure that is imposed on the bubble increases as the bubble grows at the vortex axis, the "corrected" spherical model described in Section 3.11(averaging the field pressure on the bubble surface) was then applied to determine the inception number for each case. Figure 5 shows the bubble radius variation and the acoustic pressure for R_0=50μm and σ=4.471 in the small-scale case (one of the cases in Figure 4).

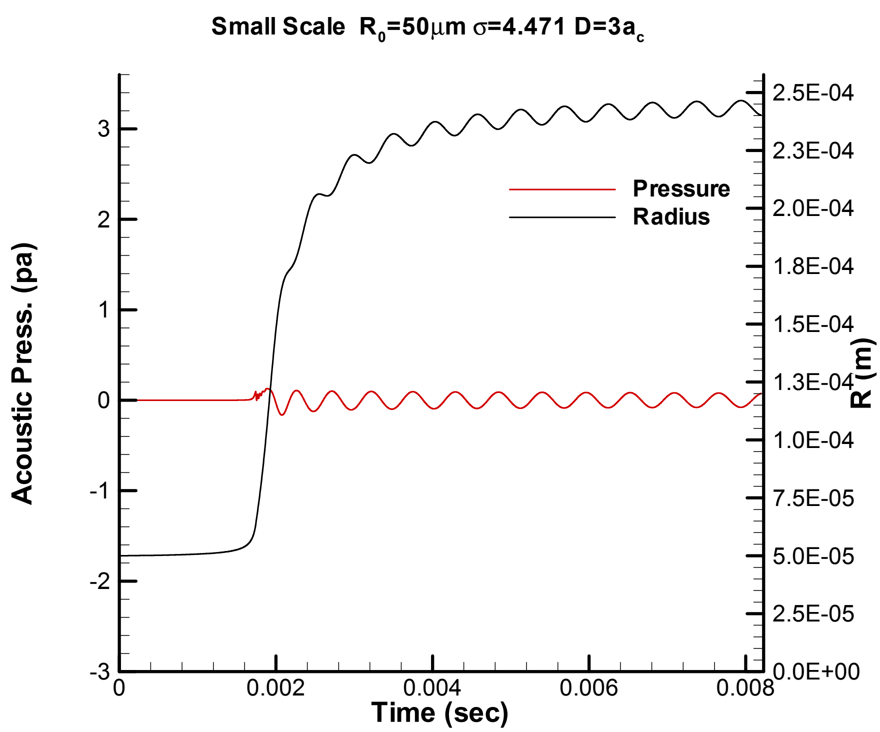

Figure 5. Bubble radius versus time and generated acoustic pressure at a distance of 30 cm. using the "modified" Rayleigh-Plesset equation (bubble released at 3a$_c$)

It is seen that with the modified model both the bubble size and the acoustic pressure reach finite values instead of increasing unboundedly. Therefore, we conducted with this modification a series of computations to obtain the maximum values of the bubble size and the acoustic pressure for different cavitation numbers. To reduce the computational time, all the computations were conducted with a closer release location than in Figures 4 and 5, D=0.5a_c.

To consider the effect of varying the release location on the results, we consider the following. The same bubble size, 50 µm is released at 0.5 a_c with the assumption that the initial size corresponds always to the local static equilibrium. Figure 6 shows the corresponding bubble radius variation and the acoustic pressure. Compared to Figure 5, one can see that the maximum bubble size and acoustic pressure are smaller for the bubble released at D=0.5a_c. This is because the bubble released at D=0.5a_c actually contains more gas (is effectively smaller) than the 50µm bubble released at D=3a_c. To correct for this we use the static equilibrium at both release locations and at the free stream location, and correct the initial bubble size, R_0, at the selected release location by solving

$$R_0^3 + \left(2\frac{\gamma}{p_w - p_v}\right)R_0^2 - \left(p_\infty \frac{R_\infty^3}{p_w - p_v}\right) = 0\,, \tag{4.3}$$

where R_∞ is the bubble size at infinity.

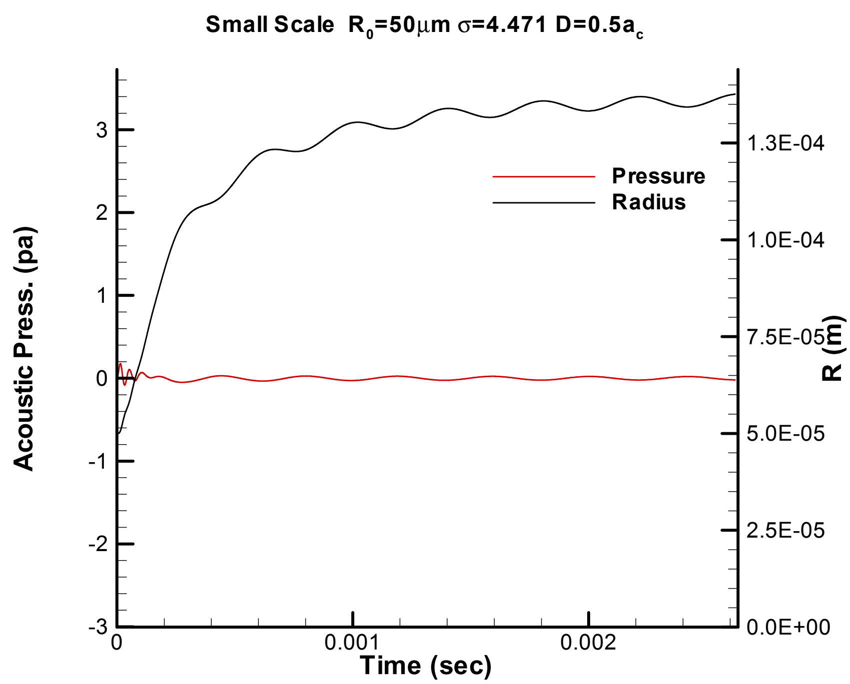

Figure 6. Bubble radius versus time and generated acoustic pressure at a distance of 30 cm. using the "modified" Rayleigh-Plesset equation (bubble released at 0.5a_c)

If Equation (4.3) is applied to correct the initial bubble size to simulate the same nuclei (R_0=50µm) at D=3a_c, one will have R_0=96.8µm and the bubble radius variation and the acoustic pressure become as shown in Figure 7. One can see that although both the maximum bubble size and acoustic pressure are now closer to those of Figure 5, a slight over-correction is found due to the neglect of dynamic effects when deriving Equation (4.3).

From here on we will apply such a correction to the initial bubble size if we do any comparisons between two different initial release locations.

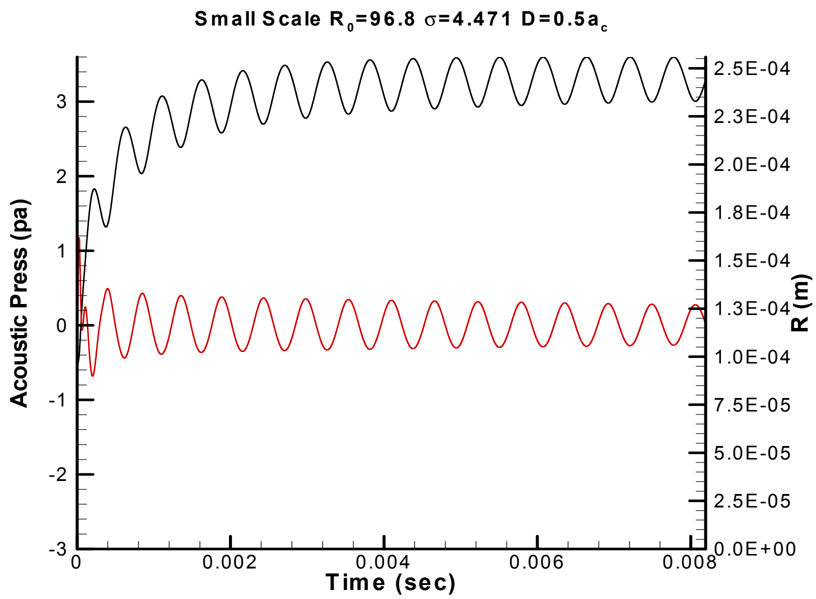

Figure 7. Bubble radius versus time and generated acoustic pressure at a distance of 30 cm. using the "modified" Rayleigh-Plesset equation (The bubble of an initial radius of 96.8 μm and released at 0.5a_c is equivalent to the 50 μm bubble of Figure 5 released at 3a_c)

Figures 8-10 show the maximum bubble size and acoustic pressure measured at 30cm from the vortex center versus the cavitation number for four different initial nuclei sizes (R_0=10, 25, 50 and 100μm) and for the three scales: small, medium and large. All the computations were conducted by releasing the bubble at D=0.5a_c. It is important to note that the curve of maximum bubble radius for R_0=10μm in the small scale is flat, i.e. the bubble does not have explosive growth even for the smallest cavitation number considered. From previous studies (Chahine and Shen 1986), it is known that for bubbles to have explosive growth the encountered pressure must be smaller than the critical pressure. Since the current model assumes that the pressure in the flow field cannot become negative, the bubble will not have an explosive growth if its critical pressure is negative.

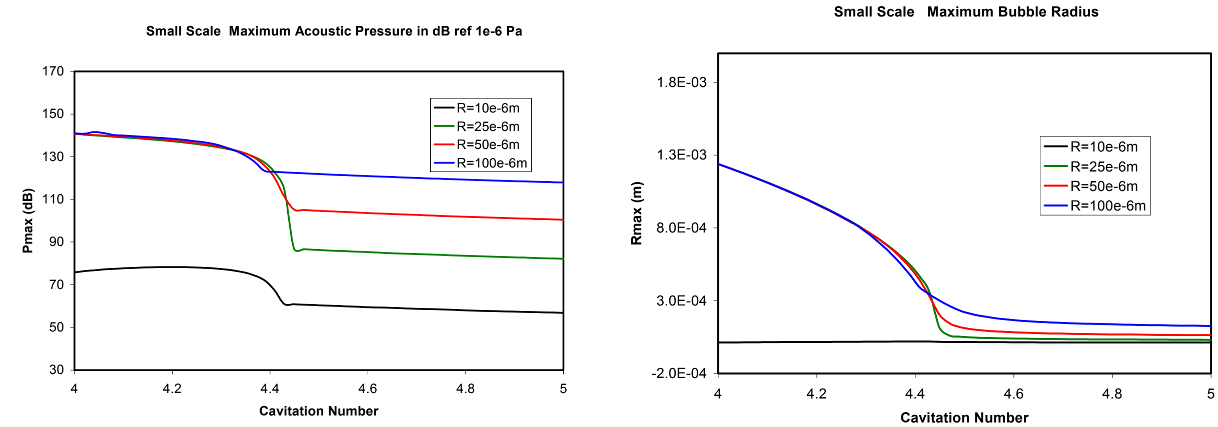

Figure 8. Maximum Bubble radius, and maximum emitted pressure as a function of the cavitation number for a constant core size. Small Scale.

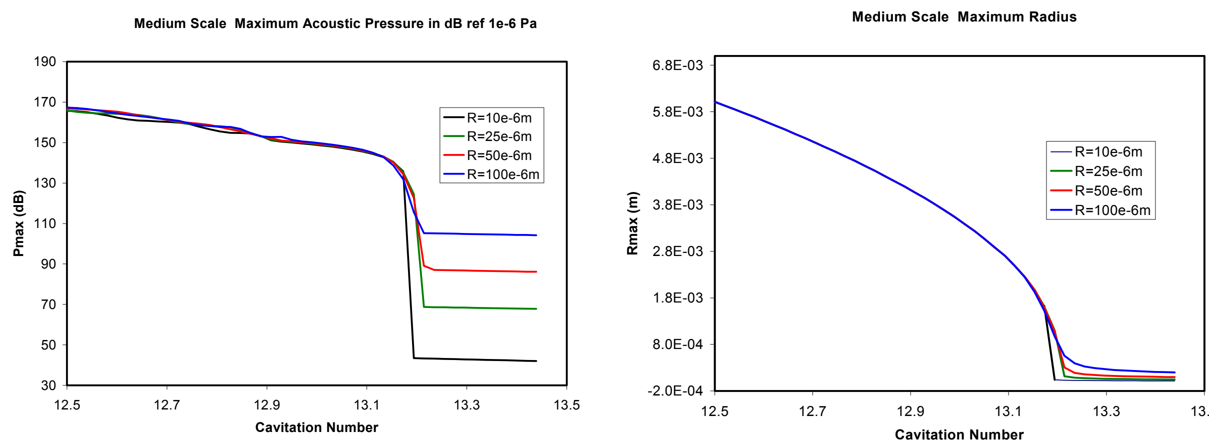

Figure 9. Maximum Bubble radius, and maximum emitted pressure as a function of the cavitation number for a constant core size. Medium Scale.

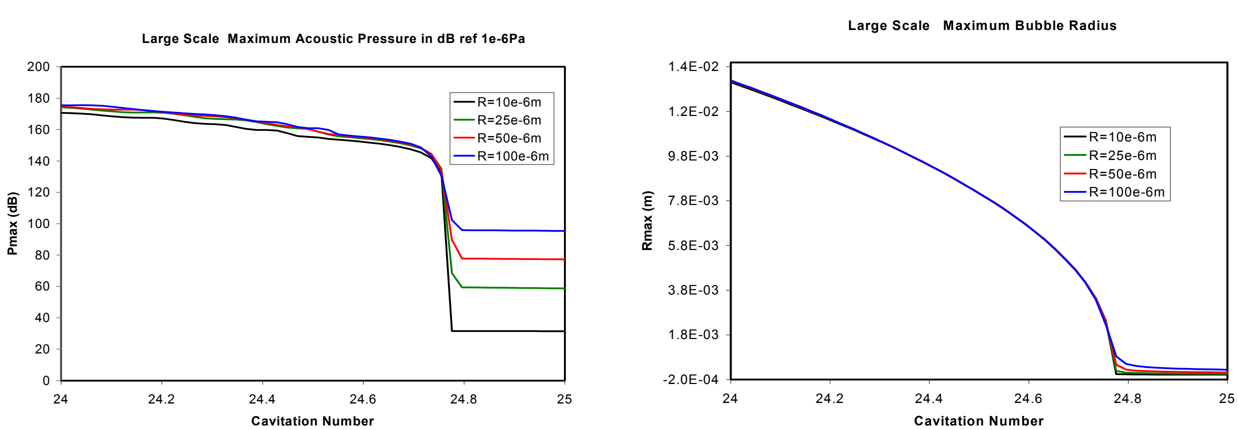

Figure 10. Maximum Bubble radius, and maximum emitted pressure as a function of the cavitation number for a constant core size. Large Scale.

Based on these curves one can determine the cavitation inception number once the optical or acoustic threshold criterion is defined. Tables 3 and 4 show examples of the cavitation inception number results obtained for all scales using different illustrative criteria. It is seen that different cavitation inception criteria may lead to significant differences in the resulting cavitation inception numbers. It is also found that the initial nucleus size, R_0, can significantly influence the prediction of the cavitation inception number. For *stringent* (very good detection schemes) acoustic or optical criteria (*e.g.* P_{max}>90db or R_{max}>100µm), the cavitation inception numbers are definitely not well scaled by Equation (4.2) especially for the smaller nuclei. However, for *looser* (high levels needed for detection) criteria (*e.g.* P_{max}>130db or R_{max}>400µm), we find that the cavitation inception number is insensitive to the nuclei size and is generally well scaled by Equation (4.2).

ACOUSTIC CRITERION		**Small Scale**	**Medium Scale**	**Large Scale**
$-Cp_{min}$		**4.47**	**13.22**	**24.80**
P_{max} > 90db;	R_0 = 10µm	No Inception	σ_i = 13.20	σ_i = 24.76
	R_0 = 25µm	σ_i = 4.45	σ_i = 13.21	σ_i = 24.77
	R_0 = 50µm	σ_i > 7	σ_i = 13.21	σ_i = 24.78
	R_0= 100µm	σ_i > 9	σ_i > 15	σ_i > 26
P_{max}> 130db;	R_0 = 10µm	No Inception	σ_i = 13.17	σ_i = 24.76
	R_0 = 25µm	σ_i = 4.36	σ_i = 13.18	σ_i = 24.76
	R_0 = 50µm	σ_i = 4.36	σ_i = 13.18	σ_i = 24.76
	R_0= 100µm	σ_i = 4.37	σ_i = 13.19	σ_i = 24.76

Table 3. Cavitation inception index obtained using various illustrative acoustic criteria for calling inception and the "improved" spherical model approach

OPTICAL CRITERION		Small Scale	Medium Scale	Large Scale
$-Cp_{min}$		**4.47**	**13.22**	**24.80**
R_{max}> 100μm	R_0 = 10μm	No Inception	σ_i = 13.20	σ_i = 24.77
	R_0 = 25μm	σ_i = 4.45	σ_i = 13.23	σ_i = 24.82
	R_0 = 50μm	σ_i = 4.51	σ_i = 13.42	σ_i > 25
	R_0= 100μm	σ_i > 5	σ_i > 14	σ_i > 25.5
R_{max}> 400μm	R_0 = 10μm	No Inception	σ_i = 13.19	σ_i = 24.78
	R_0 = 25μm	σ_i = 4.41	σ_i = 13.21	σ_i = 24.78
	R_0 = 50μm	σ_i = 4.41	σ_i = 13.21	σ_i = 24.78
	R_0= 100μm	σ_i = 4.42	σ_i = 13.23	σ_i = 24.82

Table 4. Cavitation inception index obtained using various illustrative optical criteria for calling inception and the "improved" spherical model approach

Figure 11 shows the amplitude spectrum obtained from the Fourier transform of the acoustic pressure for R_0=50μm and σ = 4.471 in the small-scale case when the bubble is released at the two locations.

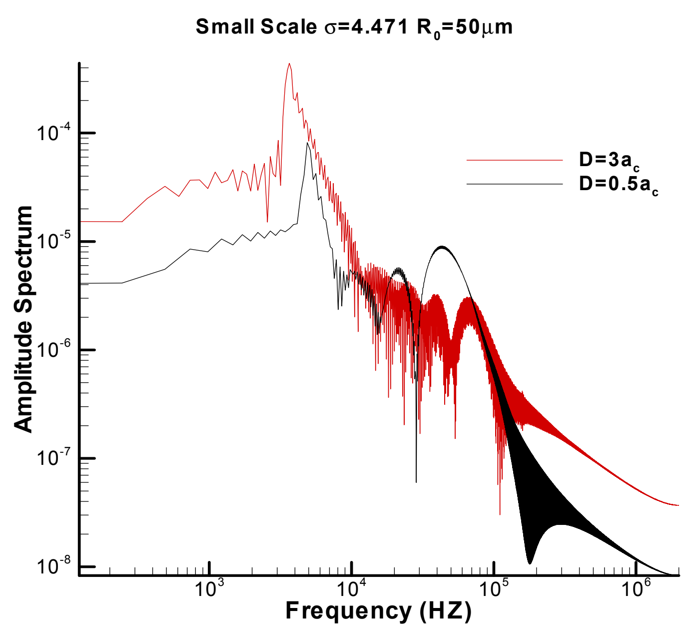

Figure 11. Influence of the location of initial bubble release on the amplitude spectrum of the emitted sound.

4.4 Effect of Vortex Core Diffusion

4.4.1 Bubble Dynamics

In the previous section the pressure along the vortex axis was assumed to remain constant. This allowed the bubble to reach some equilibrium status after reaching the vortex center. Therefore, the acoustic emission in this case was mainly from the bubble growth and subsequent oscillations. The bubble collapse, however, is commonly known to generate most of the cavitation acoustic noise and occurs after the grown bubble encounters an adverse pressure gradient during its motion. To account for this effect, a diffusive line vortex was specified by taking into account vortex core radius decrease along the vortex axis as shown in Figure 12. The circulation of the vortex was kept constant. Figure 13 shows the resulting bubble radius variations and the acoustic pressure versus time during the bubble capture for R_0=50μm and σ= 4.471 in the small-scale case.

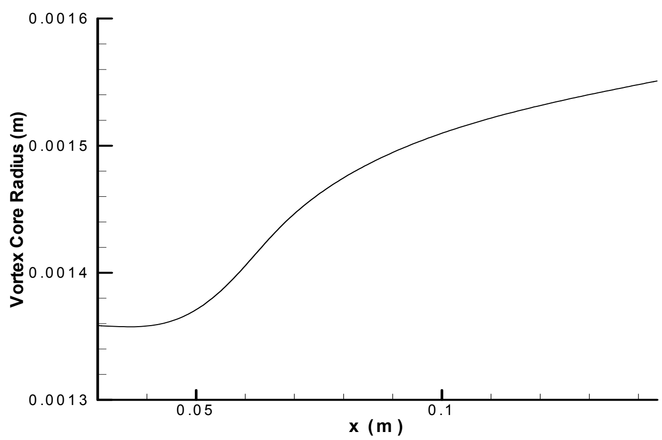

Figure 12. Diffusion of the vortex core through increase of its radius along the longitudinal direction.

It is seen that the bubble grows significantly then collapses when it encounters the adverse pressure gradient. Due to the presence of gas in the bubble and to the absence of acoustic energy loss due to liquid compressibility it pursues many successive oscillations. This leads to high frequency oscillations and stronger acoustic emission than that generated during growth. It is interesting to isolate the importance of the slip-velocity term in Equation (3.3). The result for neglecting the slip-velocity term is shown in Figure 14. One can see that stronger bubble oscillations occur in this case resulting in extremely high acoustic noise during multiple collapses.

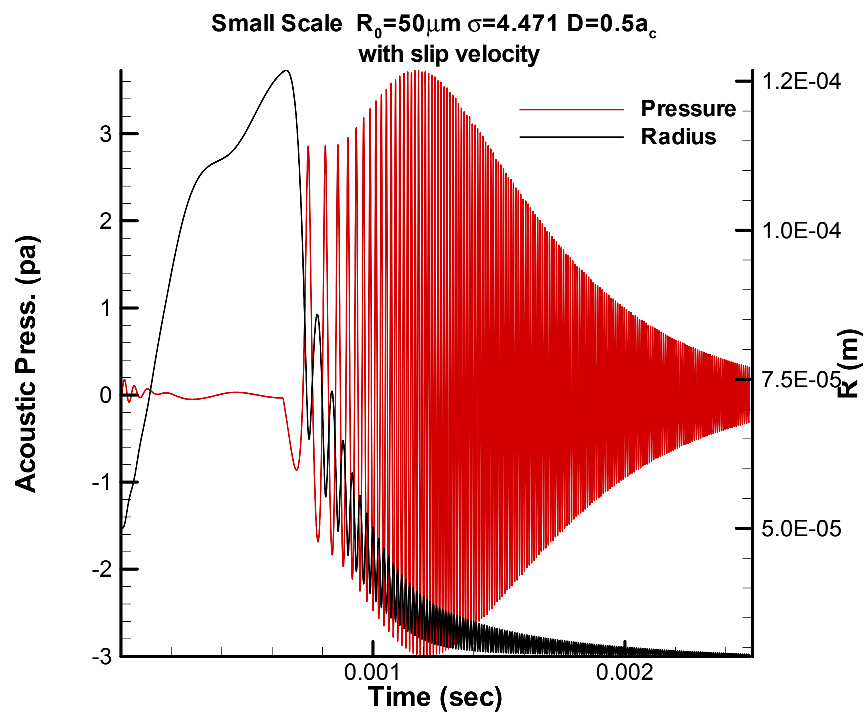

Figure 13. Bubble radius versus time and resulting acoustic pressure in a vortex line with diffusion.

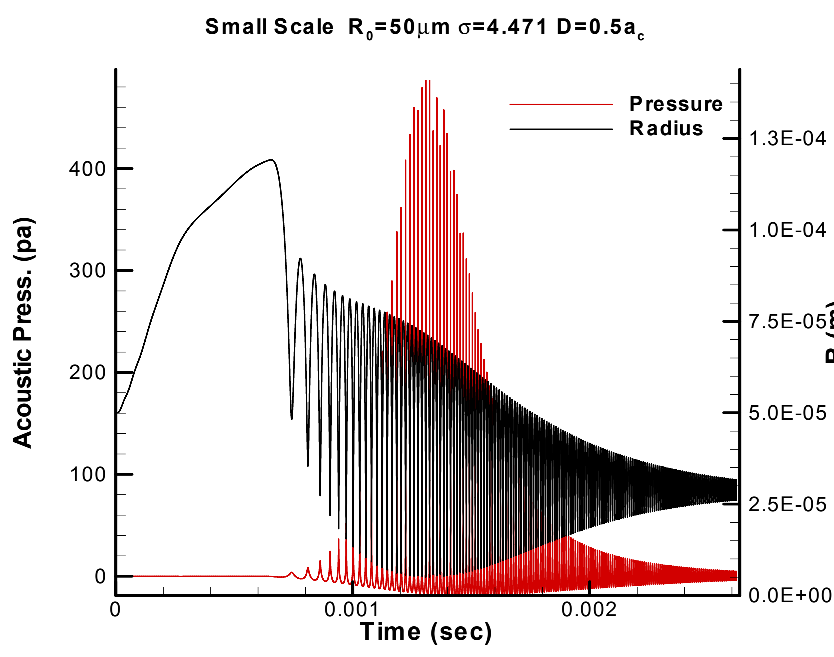

Figure 14. Bubble radius versus time and resulting acoustic pressure in a vortex line with diffusion when bubble slip velocity effects are neglected (same conditions as in Figure 13.)

4.4.2 Bubble Trajectory

It is also interesting to see how the bubble collapse influences the trajectory. From Equation (3.8) we know that the rate of change of the bubble volume is important to the trajectory when variation rate is large. The bubble growth generates a force, which impedes the bubble motion along its trajectory while the bubble collapse generates a force, which will speed up the bubble in the direction of its motion. For the spiral motion, one can expect that the bubble growth helps the bubble entrapment while the bubble collapse acts in the opposite way. Figure 15 shows that the spiral-like bubble trajectory influenced by the strong collapse during capture by the line vortex for R_0=100μm and σ = 13.215 in the middle-scale case. From Figure 16, which represents the same phenomenon in a different way, we can see that the bubble moves away from the vortex center when the very first bubble collapse occurs. It then returns and the cycle repeats.

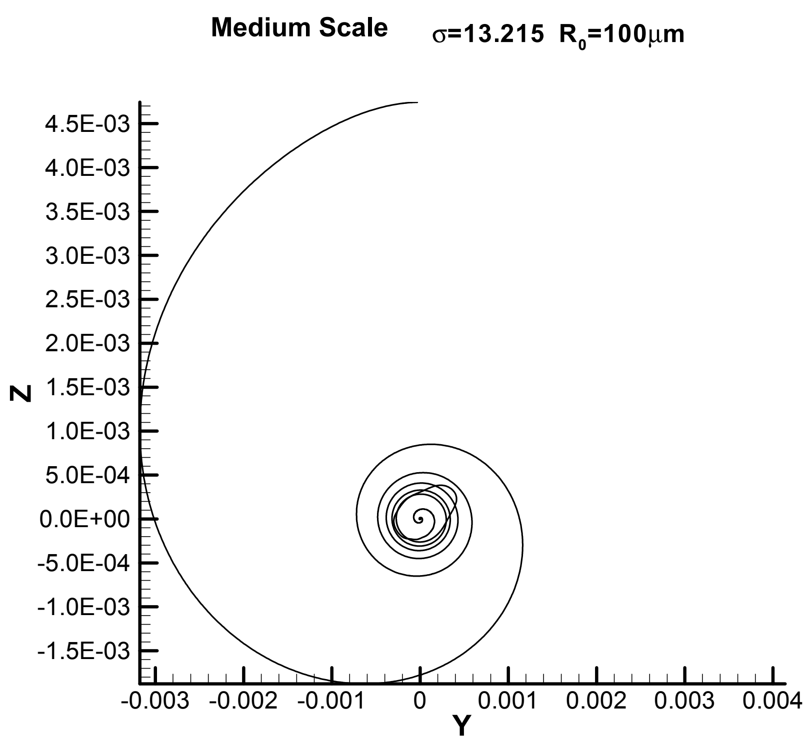

Figure 15. Bubble helicoidal trajectory during its capture by the diffusive vortex showing deviation from the helicoidal motion at the bubble collapses.

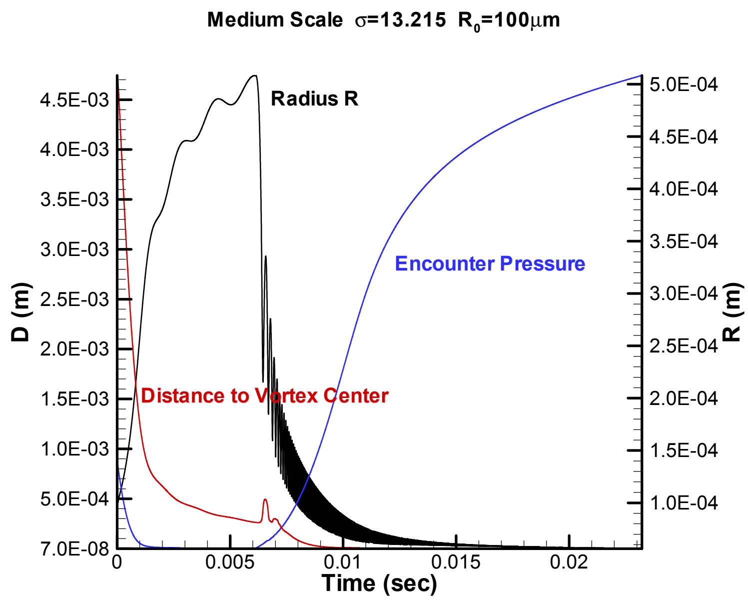

Figure 16. Bubble radius versus time and corresponding encounter pressure and motion towards the vortex line axis. Distance to the axis versus time shows repulsion at the successive bubble collapses.

4.4.3 Frequency Spectra

Figure 17 compares the acoustic signals of both constant and diffusive core cases in the frequency domain. One can see that in the diffusive core case the higher frequencies have much higher amplitudes when compared to the constant vortex core case. It is important to note that the frequency of the oscillations increases with successive collapses. This can be more clearly seen using wavelet and Hilbert transformations (See Appendix) as illustrated by Figure 18.

In order to understand this continuous increase in the frequency, we conduct an order of magnitude analysis of the expected bubble oscillations frequency based on the Rayleigh Period T,

$$F = \frac{1}{2}T^{-1} = \frac{1}{2R}\sqrt{\frac{\Delta p}{\rho}}. \tag{4.4}$$

Figure 19 shows F versus time computed using two different definitions of Δp . The blue curve was obtained by using $\Delta p = p - p_v$, while the red curve was obtained by using $\Delta p = p - p_v - p_g + 2\gamma/R$. p is the pressure seen by the bubble during its trajectory, and will be dubbed, $p_{encounter.}$ Both graphs show an initial increase of the frequency with time; however, the red curve reaches a maximum that is not seen in the wavelet or Hilbert spectra in Figure 16.

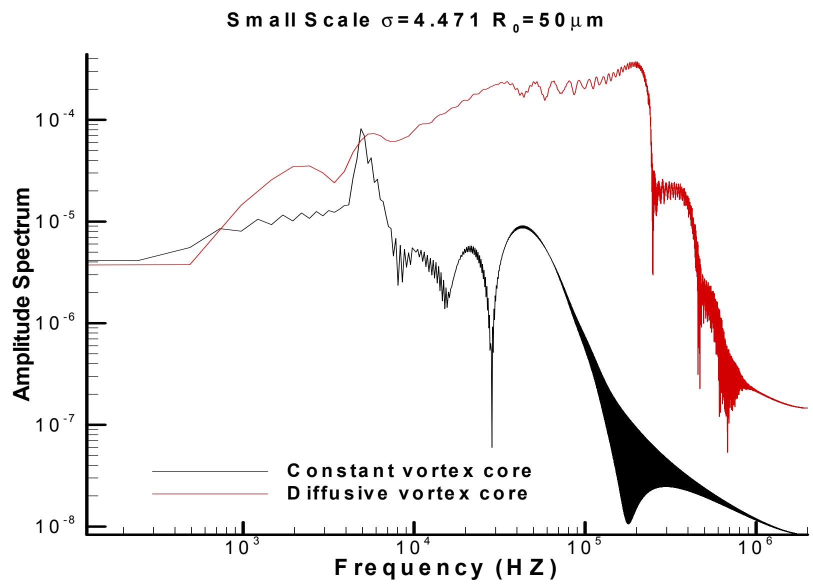

Figure 17. Comparison of the amplitude spectra of the acoustic pressure generated in a constant and a diffusive vortex core for a 50mm bubble in the small-scale numerical test.

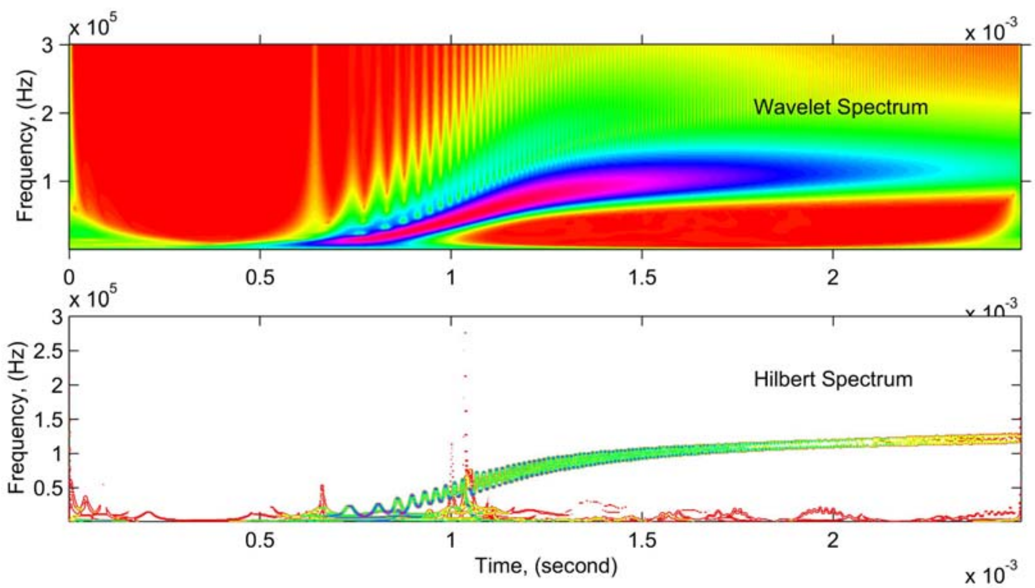

Figure 18. Wavelet and Hilbert transforms of the acoustic pressure generated in a constant and a diffusive vortex core for a 50mm bubble in the small-scale numerical test.

Using

$$F_i = \frac{1}{2R_{\max,i}}\sqrt{\frac{P_{encouter} - P_v}{\rho}}, \tag{4.5}$$

appears to give a very good approximation of the frequency of the acoustic signals.

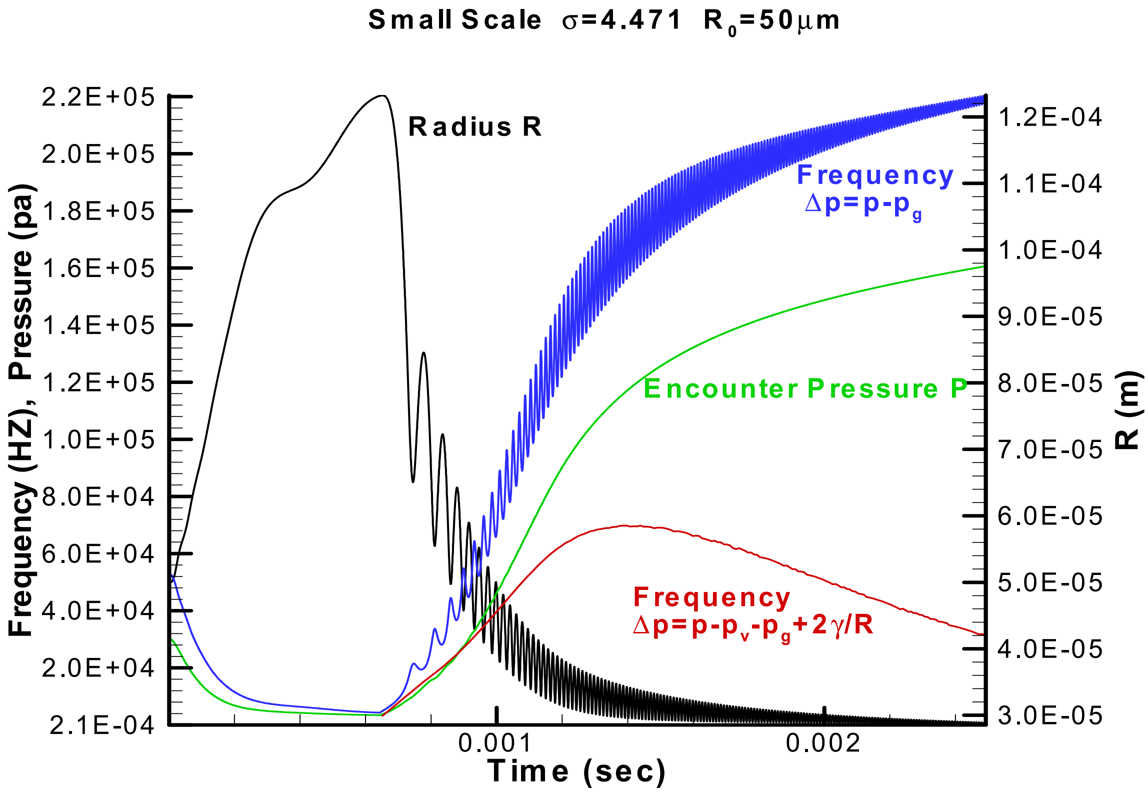

Figure 19. Bubble radius and encounter pressure versus time for a 50mm bubble. Blue curve gives the order of magnitude of the generated frequency using Equation (4.5). Red curve gives the order of magnitude of the generated frequency using Equation (4.4) with $\Delta p = p - p_v - p_g + 2\gamma / R$..

4.4.4 Influence of the initial Bubble Radius and of the Cavitation Index

One should note that for the constant vortex core case the bubble will always reach the minimum pressure inside the vortex core axis as long as the computational domain and time is large enough. Unlike in the constant vortex core case, bubbles with small initial size may not be able to enter the vortex center before the vortex core starts to diffuse. In such a case the bubble may not grow enough and then experience a strong collapse, which requires that the bubble grows to some large size relative to the initial size. Figure 20 shows the bubble radius variation and the acoustic pressure versus time during capture for R_0=10μm and σ = 4.471 in the small-scale case. Compared to Figure 13, one can see a very different bubble collapse between R_0=10μm and 50μm.

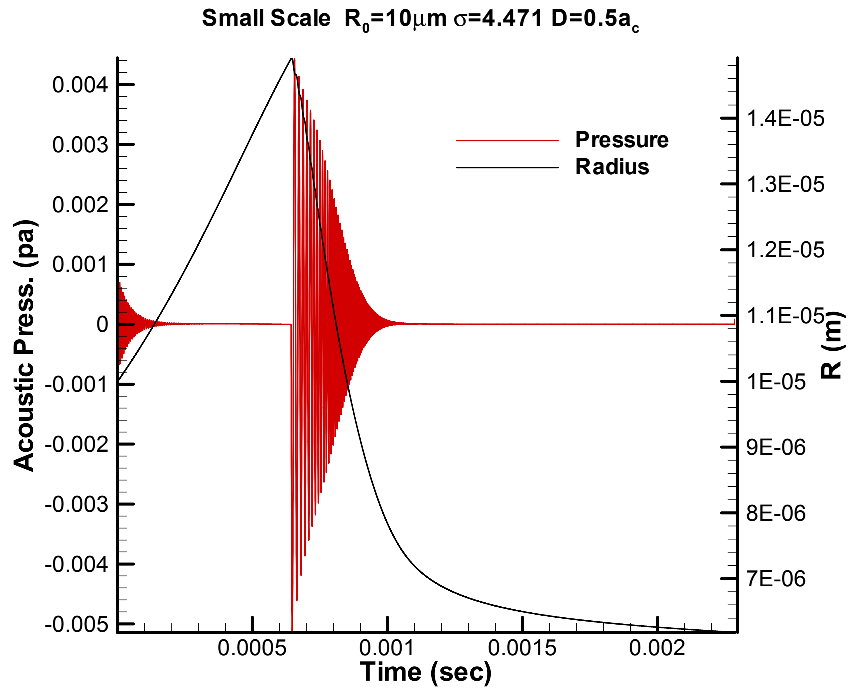

Figure 20. Small bubble size behavior. Bubble radius variations and acoustic pressure versus time during capture for R_0=10μm and σ= 4.471 in the small-scale case

As the bubble's initial size is increased, the maximum growth size that the bubble can reach is increased. As a result, when the bubble collapses, the amplitude of the acoustic pressure increases for the larger bubbles but the frequency decreases. For example, Figures 21-23 show the bubble radius variation and the acoustic pressure versus time during capture for different R_0 at σ = 4.471 in the small-scale case. By comparing Figures 20-23, one can see three major types of behavior of the bubble collapse. For small-sized bubbles, the bubble collapses without strong volume rebound and generates very high frequency but very low amplitude noise. For mid-sized bubbles, the bubble collapses with strong volume rebound and generates high frequency and high amplitude noise. For large-sized bubbles, the frequency of the bubble collapse is close to that of the bubble growth. These three different behaviors are also found in the medium and large scales.

By changing the cavitation number for the same nuclei size, one can also find these same three different behaviors. Examples are shown in Figures 24-26 for R0=10µm at different cavitation numbers in the large scale.

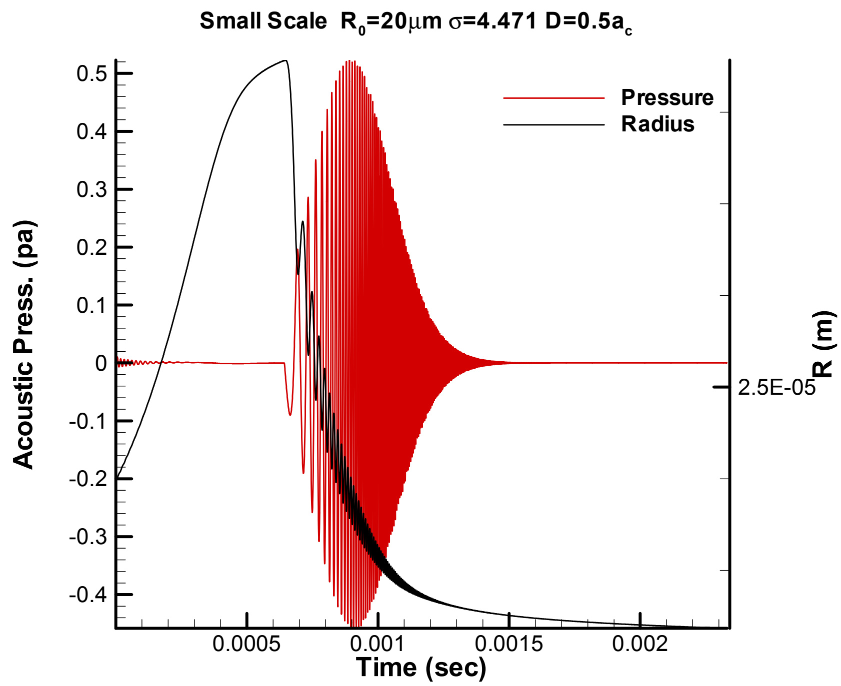

Figure 21. Small bubble size behavior. Bubble radius variations and acoustic pressure versus time during capture for R_0=20µm and σ= 4.471 in the small-scale case

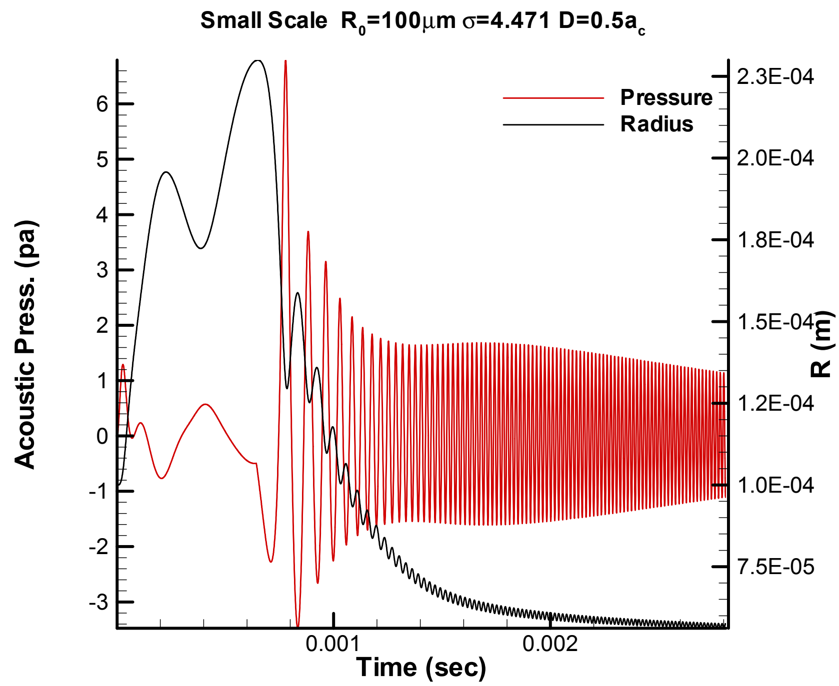

Figure 22. Medium bubble size behavior. Bubble radius variations and acoustic pressure versus time during capture for R_0=100μm and σ = 4.471 in the small-scale case

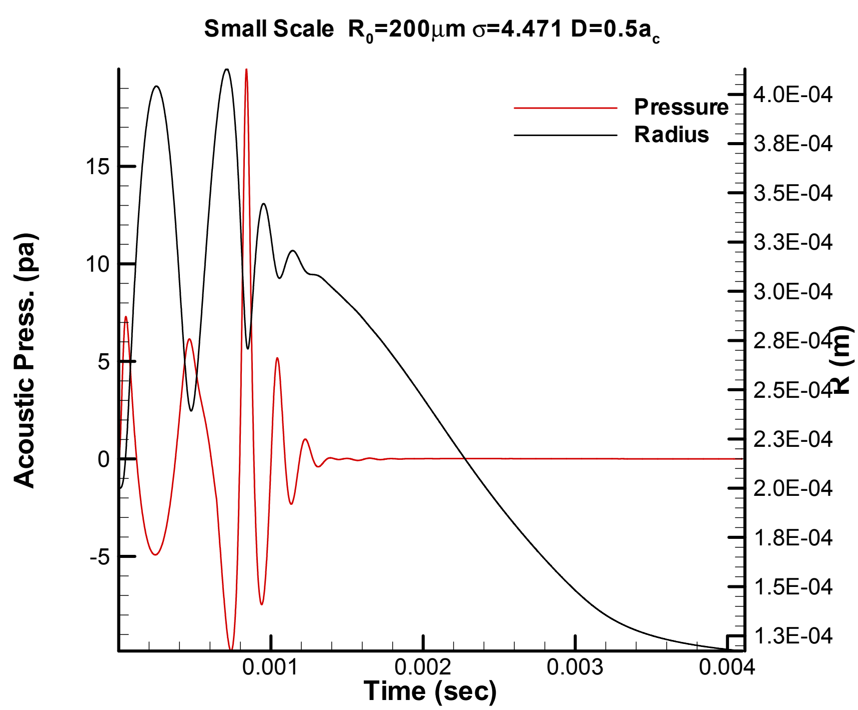

Figure 23. Large bubble size behavior. Bubble radius variations and acoustic pressure versus time during capture for R_0=200μm and σ = 4.471 in the small-scale case

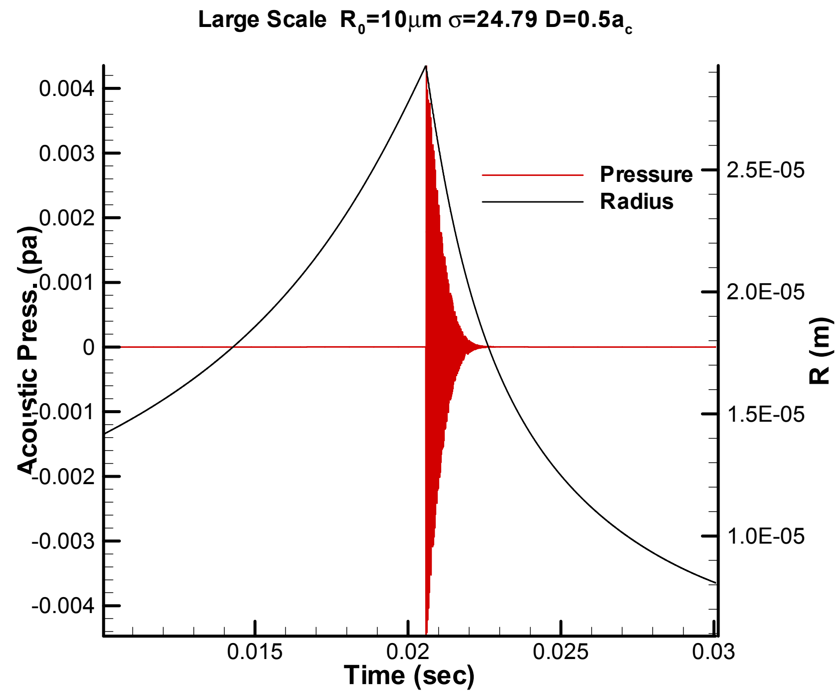

Figure 24. Bubble behavior for high cavitation numbers. Bubble radius variations and acoustic pressure versus time during capture for R_0=10μm and σ= 24.79 in the large-scale tests.

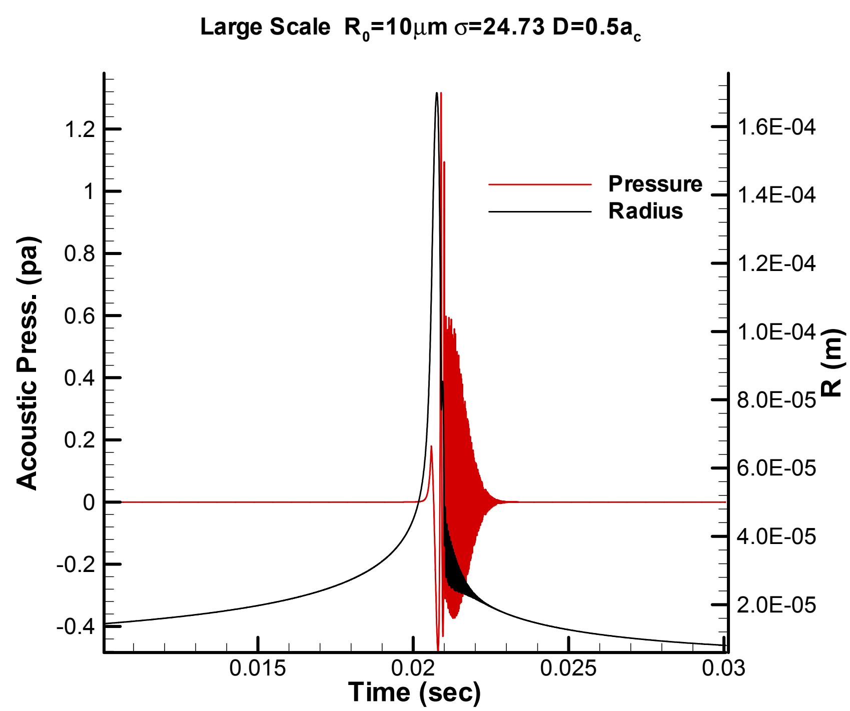

Figure 25. Bubble behavior for average cavitation numbers. Bubble radius variations and acoustic pressure versus time during capture for R_0=10μm and σ= 24.73 in the large-scale tests.

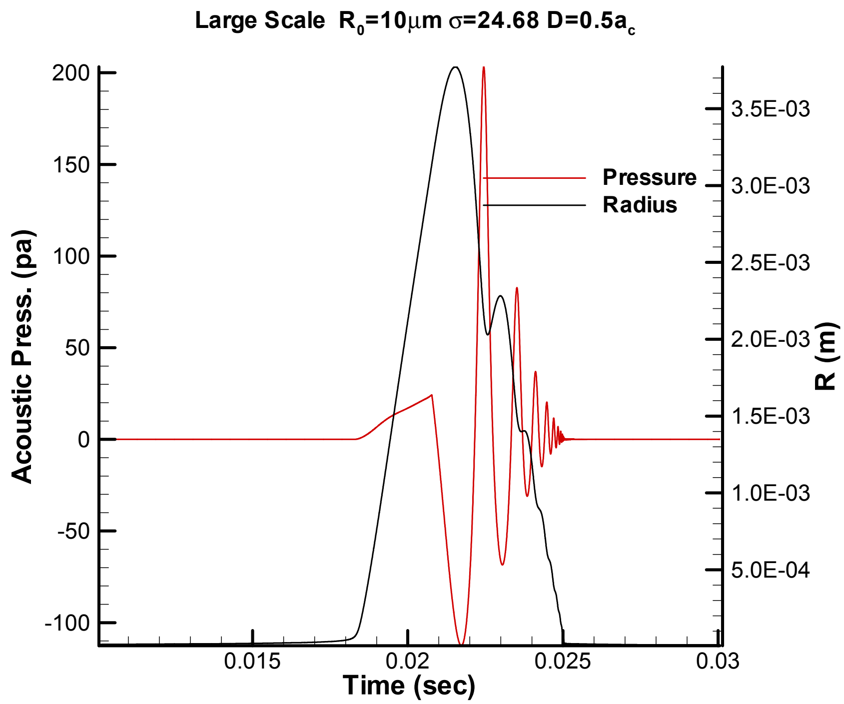

Figure 26. Bubble behavior for low cavitation numbers. Bubble radius variations and acoustic pressure versus time during capture for R_0=10μm and σ= 24.68 in the large-scale tests.

4.3.2 Scaling of Tip Vortex Cavitation Inception

A series of computations similar to those in the previous section were conducted to obtain the maximum size of the bubble and the maximum acoustic pressure versus the cavitation number. Three initial nuclei sizes (R_0=10, 50 and 100μm) were used for all three scales. Figures 27-29 show that the maximum bubble size and the maximum acoustic pressure measured at 30 cm from the vortex center at the release location versus the cavitation number for the small, medium, and large scales. These curves were also obtained by releasing the bubble at 0.5a_c from the vortex center. It is seen that the maximum radius curves are not significantly different from those of constant core case for larger initial bubble sizes (R_0=25, 50 and 100μm) for σ>4.38 in the small scale. Below σ=4.38 the values of maximum radius increase abruptly. By checking the trajectory of the bubble (e.g. see Figure 30 for R_0=50μm at σ=4.38 in the small scale), one can find that the bubble becomes trapped longitudinally on the vortex axis due to the presence of the adverse pressure gradient, $\partial p/\partial x$, at the stream wise location where the vortex diffusion starts to occur. This allows the bubble to grow to a much larger size because the effect of slip velocity is significant.

The bubble, however, is not trapped for the medium and large scales (Figures 28 and 29) because the adverse pressure gradient force is not large enough in these cases to stop the bubble downstream motion. As a result, the maximum radius curves for larger initial bubble sizes (R_0=25, 50 and 100μm) in the medium and large scales are very close to those of the constant vortex core case. For the smaller initial bubble size (R_0=10μm), however, the curves are significantly different from those of constant vortex core because the bubble with smaller initial size may not be able to enter the vortex center before the vortex core diffuses. To allow the smaller initial bubble size to enter the vortex center before the vortex core diffuses, further decreases of the cavitation number are required. Unlike the maximum radius curves, the maximum acoustic pressure curves of diffusive vortex core are all differ significantly from those of the constant vortex core, except at high cavitation numbers where the acoustic signal created by the bubble collapse is not stronger than that of growth.

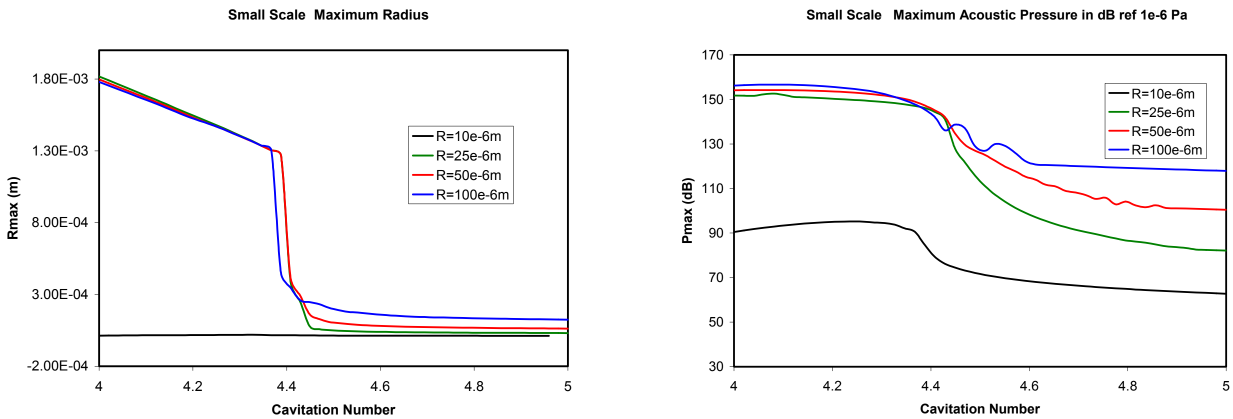

Figure 27. Maximum Bubble radius, and maximum emitted pressure as a function of the cavitation number for a diffusive vortex. Small Scale.

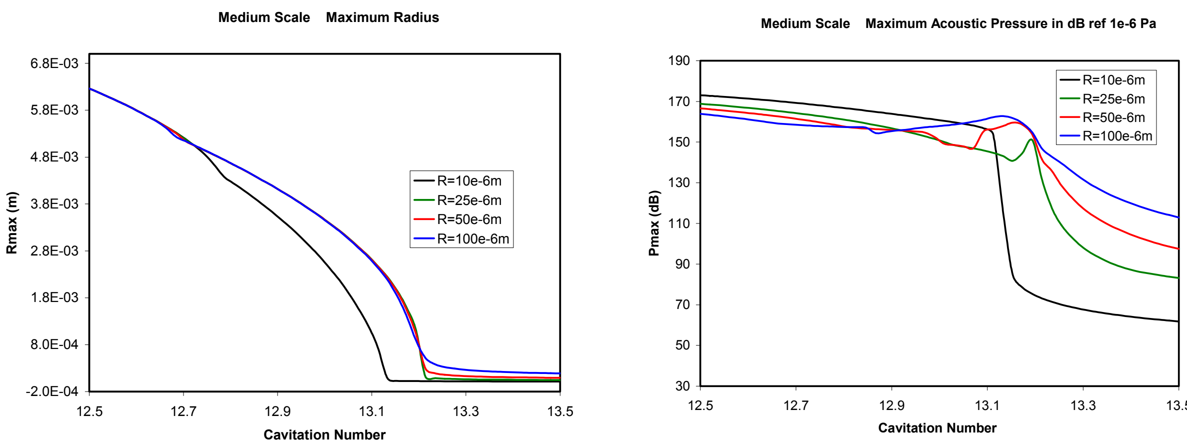

Figure 28. Maximum Bubble radius, and maximum emitted pressure as a function of the cavitation number for a diffusive vortex. Medium Scale.

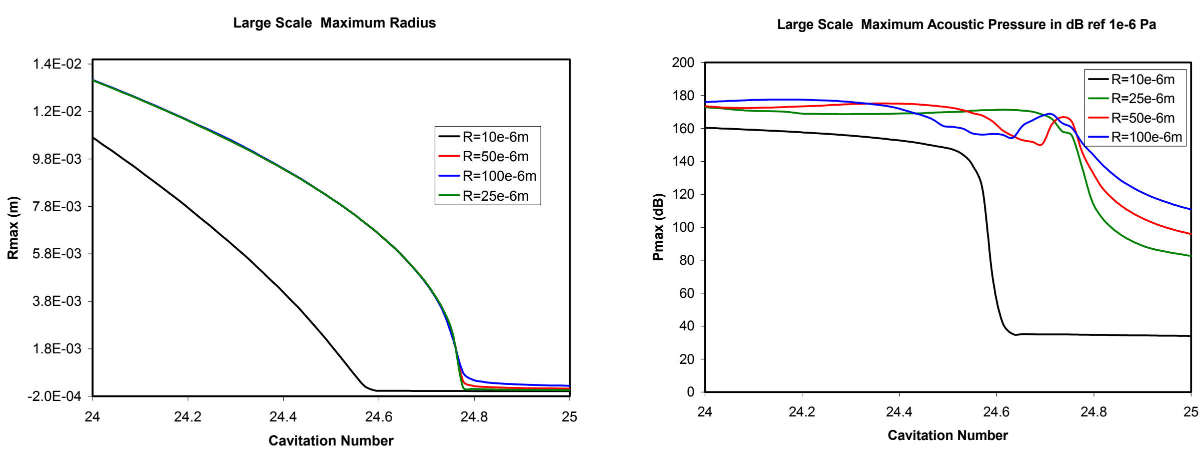

Figure 29. Maximum Bubble radius, and maximum emitted pressure as a function of the cavitation number for a diffusive vortex. Large Scale.

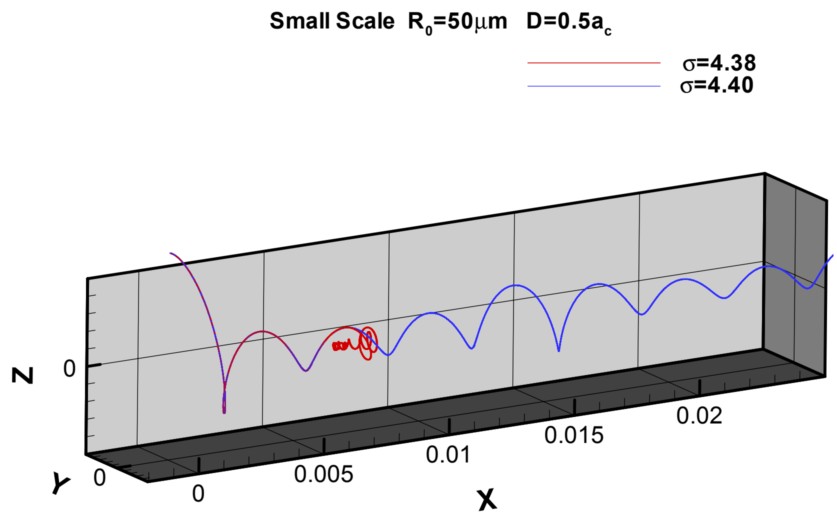

Figure 30. Trajectory of a 50 μm bubble in a diffusive vortex core indicating possibility for bubble capture at some values of sigma. This results in much greater bubble growth.

Tables 5 and 6 show the cavitation inception numbers for all the cases considered by choosing the same criteria as in Tables 3 and 4. Unlike the constant vortex core case in which one can choose appropriate acoustic and optical criteria such that the cavitation inception number can be well correlated by Equation (4.2), it is here very difficult to define such acoustic or optical criteria for the diffusive vortex core case.

ACOUSTIC CRITERION		Small Scale	Medium Scale	Large Scale
$-Cp_{min}$		**4.47**	**13.22**	**24.80**
P_{max} > 90db;	R_0 = 10μm	σ_i = 4.37	σ_i = 13.15	σ_i = 24.59
	R_0 = 25μm	σ_i = 4.71	σ_i = 13.38	σ_i = 24.88
	R_0 = 50μm	σ_i > 6	σ_i > 13.5	σ_i > 25
	R_0= 100μm	σ_i > 7	σ_i > 14	σ_i > 25.5
P_{max}> 130db;	R_0 = 10μm	No Inception	σ_i = 13.13	σ_i =24.56
	R_0 = 25μm	σ_i = 4.45	σ_i = 13.22	σ_i =24.78
	R_0 = 50μm	σ_i = 4.47	σ_i = 13.25	σ_i =24.80
	R_0= 100μm	σ_i = 4.49	σ_i = 13.32	σ_i = 24.85

Table 5. Cavitation inception index obtained using various illustrative acoustic criteria for calling inception and the "improved" spherical model approach in the case of the diffusive vortex.

OPTICAL CRITERION		Small Scale	Medium Scale	Large Scale
$-Cp_{min}$		**4.47**	**13.22**	**24.80**
R_{max}> 100μm	R_0 = 10μm	No Inception	σ_i = 13.13	σ_i= 24.59
	R_0 = 25μm	σ_i = 4.45	σ_i = 13.23	σ_i = 24.82
	R_0 = 50μm	σ_i = 4.49	σ_i > 13.5	σ_i > 25
	R_0= 100μm	σ_i > 5.5	σ_i > 14	σ_i > 25.5
R_{max}> 400μm	R_0 = 10μm	No Inception	σ_i = 13.12	σ_i = 24.56
	R_0 = 25μm	σ_i = 4.39	σ_i = 13.22	σ_i = 24.77
	R_0 = 50μm	σ_i = 4.41	σ_i = 13.22	σ_i = 24.78
	R_0= 100μm	σ_i = 4.41	σ_i = 13.24	σ_i = 24.82

Table 6. Cavitation inception index obtained using various illustrative optical criteria for calling inception and the "improved" spherical model approach in the case of the diffusive vortex.

4.5 Frequency Analysis

To study further the characteristics of the emitted noise during capture of a bubble in a vortex frequency one can apply a Fourier transformation to the pressure signals. Figures 31-33 show the Fourier spectrum for different R_0 for the small, medium and large scales. For each scale it is found that these curves can be categorized into three major groups according to their shapes.

a) In the first group, the curves show two major peaks, one obtained during bubble growth and one during the collapse phases. This group appears in all scales for smaller nuclei sizes (R_0 = 5 and 10μm).

b) In the second group, the curves show a rather flat region at the high amplitude, which is mainly due to the subsequent collapses. This group appears in the small scale for R_0 = 20, 50 and 100μm.

c) In the third group, the curves show only one major peak, which indicates the frequency of the bubble growth and collapse are very close. This is followed by a gradual classical power-law type decay of the spectrum. This group appears in the small scale for R_0 = 200 and 500μm.

These three groups can be also used to categorize the Fourier spectrum obtained for different σ with same R_0. Figure 34 shows the Fourier spectrum for different σ with R_0=10μm in the large scale.

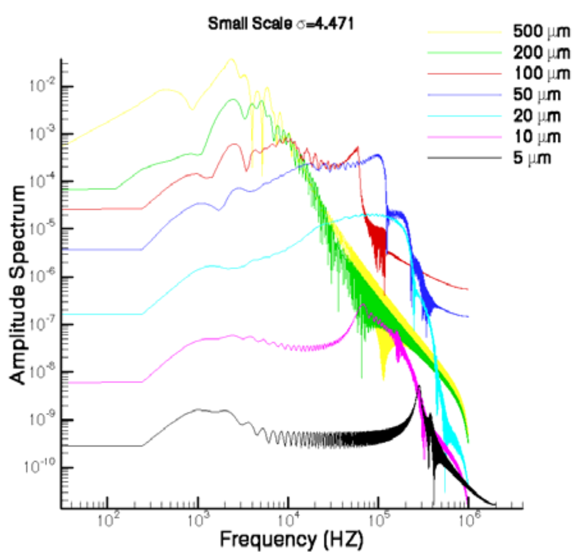

Figure 31. Amplitude spectrum for various initial nuclei sizes in the small-scale numerical tests at σ=4.471.

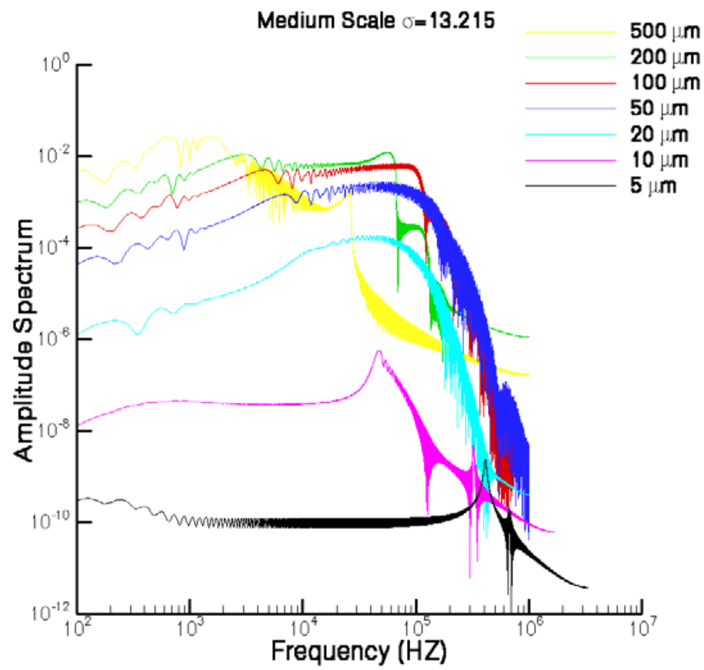

Figure 32. Amplitude spectrum for various initial nuclei sizes in the medium-scale numerical tests at σ=4.471.

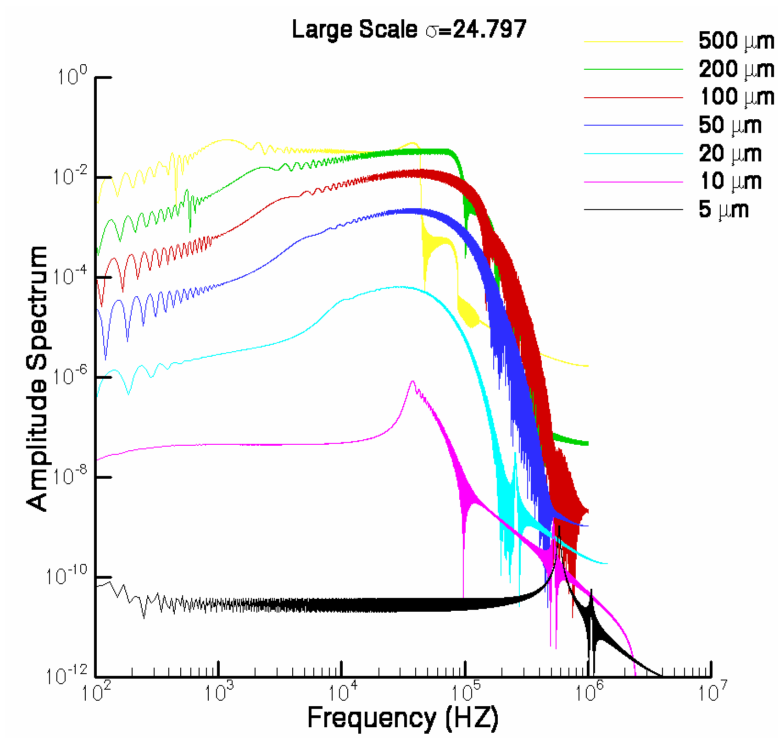

Figure 33. Amplitude spectrum for various initial nuclei sizes in the large-scale numerical tests at σ=4.471.

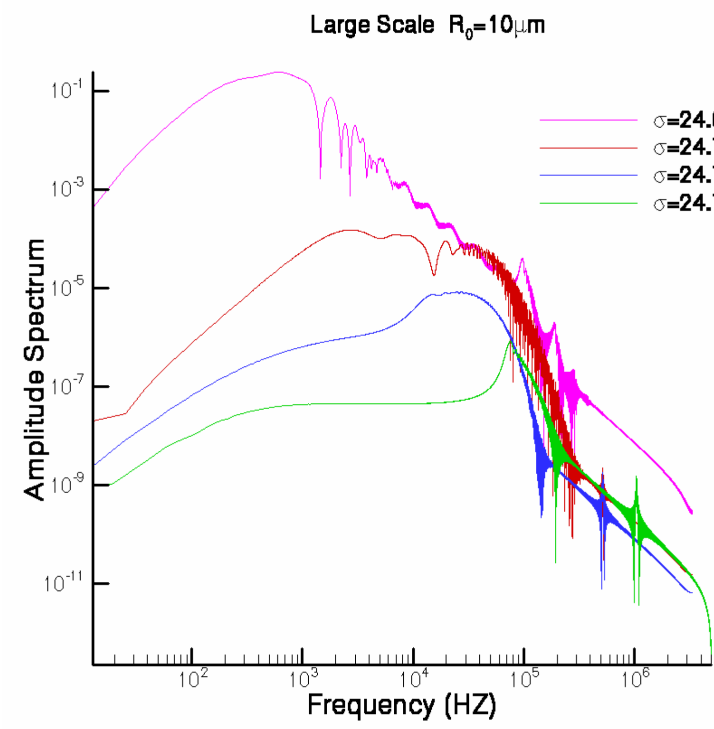

Figure 34. Amplitude spectrum for various cavitation numbers in the large-scale numerical tests and R_0=10μm.

Although the curves of the third group do not appear in the medium and large scale figures, one can expect them to occur for larger nuclei (R_0 > 500μm). In fact, the curve of 500μm in the medium scale is a transition between the second and the third group. It is important to know what the peaks in the spectral domain correspond to. To identify these peaks we can estimate the frequency at the location of interest in the acoustic signal. Figures 35 and 36 show the correspondence between time and frequency domains for two cases. Figure 35 indicates that the two peaks appearing in the frequency domain for R_0 = 10μm correspond to the acoustic signals generated at the bubble growth and collapse respectively. Although no strong peak is shown in frequency domain for R_0 = 100μm, with this estimation we can still identify the location of the signal due to the first collapse (see Figure 36).

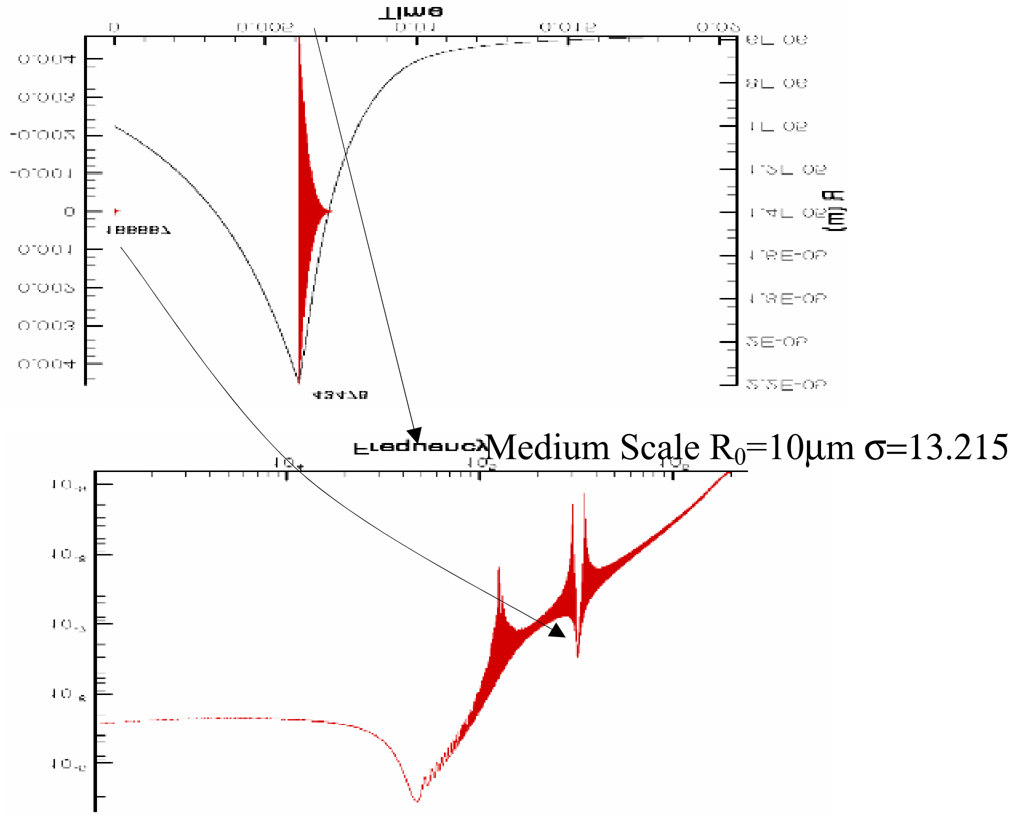

Figure 35. Correspondence between acoustic signals and the peak frequencies in the Fourier spectrum. R_0=10μm.

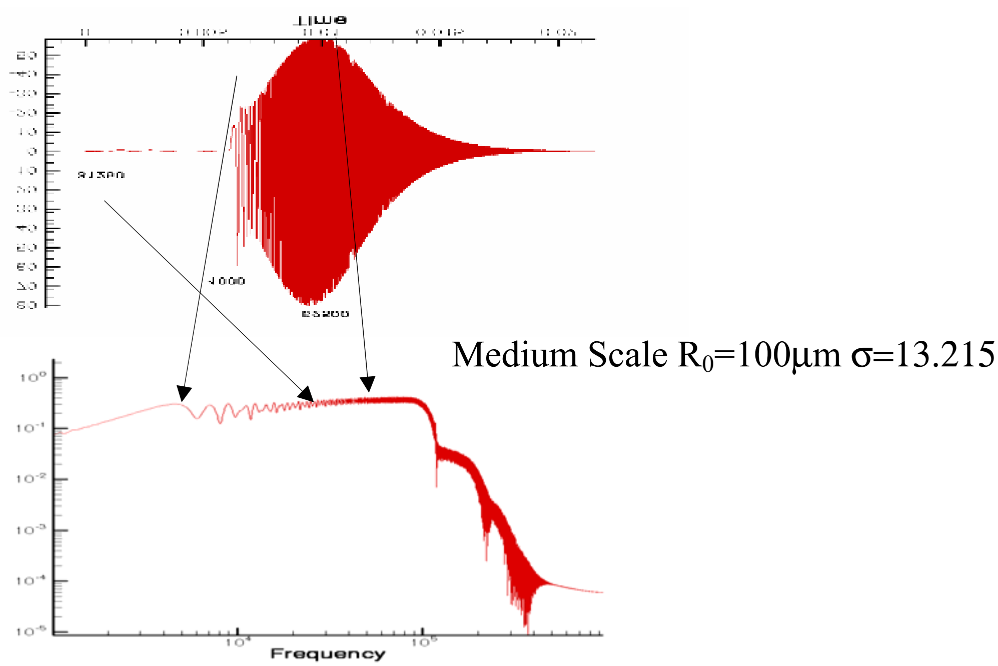

Figure 36. Correspondence between acoustic signals and the peak frequencies in the Fourier spectrum. R_0=100μm.

One disadvantage of the Fourier transformation is that it does not provide information regarding when in time the various spectral components appear. When the time localization of the spectral components is needed, either the wavelet or the Hilbert transformation can provide the time-frequency representation. Figures 37 and 38 show the frequency versus time by applying the wavelet and Hilbert transformations to the acoustic signal generated by R_0 =10μm and 100μm in the medium scale. One can see both wavelet and Hilbert transformations provide time information where the interesting spectral components appear. By checking the time when the bubble growth and first collapse occur, one can identify the frequency of the first collapse easily and have the information as shown in Figures 35 and 36.

From Equation (4.4) it is known that the frequency of the first collapse signal is controlled by the maximum radius and pressure gradient at the location where the vortex core starts to diffuse. By appropriately choosing the normalization factor one can well normalize the first collapse signal of the second group. Figures 39-41 show the spectra after normalization. The frequencies are normalized by:

$$\tau = R_m \sqrt{\frac{\rho}{\Delta P}}, \tag{4.6}$$

and the amplitude of the spectrum is normalized by:

$$A = \frac{\Delta P \tau R_m}{l} = \frac{R_m^2}{l}\sqrt{\rho \Delta P}, \tag{4.7}$$

where R_m is the maximum radius, l is the distance to the location where the acoustic signal is computed, and Δp is the difference between the encounter pressure at the first and second bubble collapse (see Figure 42 for a definition sketch).

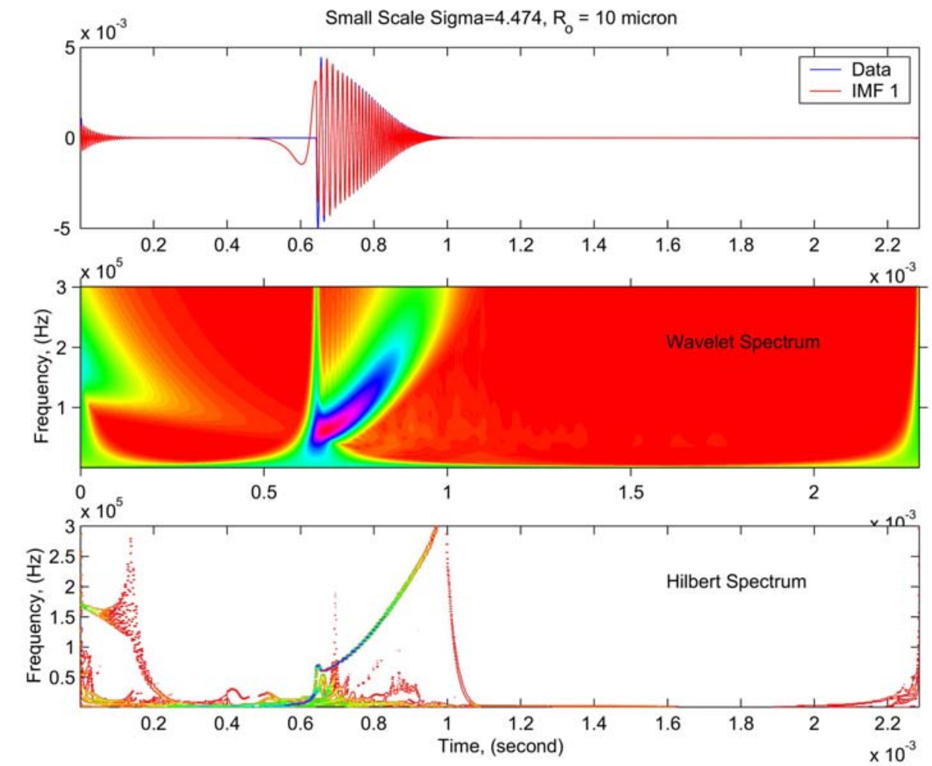

Figure 37. Pressure signal, wavelet and Hilbert transforms for a 10μm bubble in a diffusing vortex

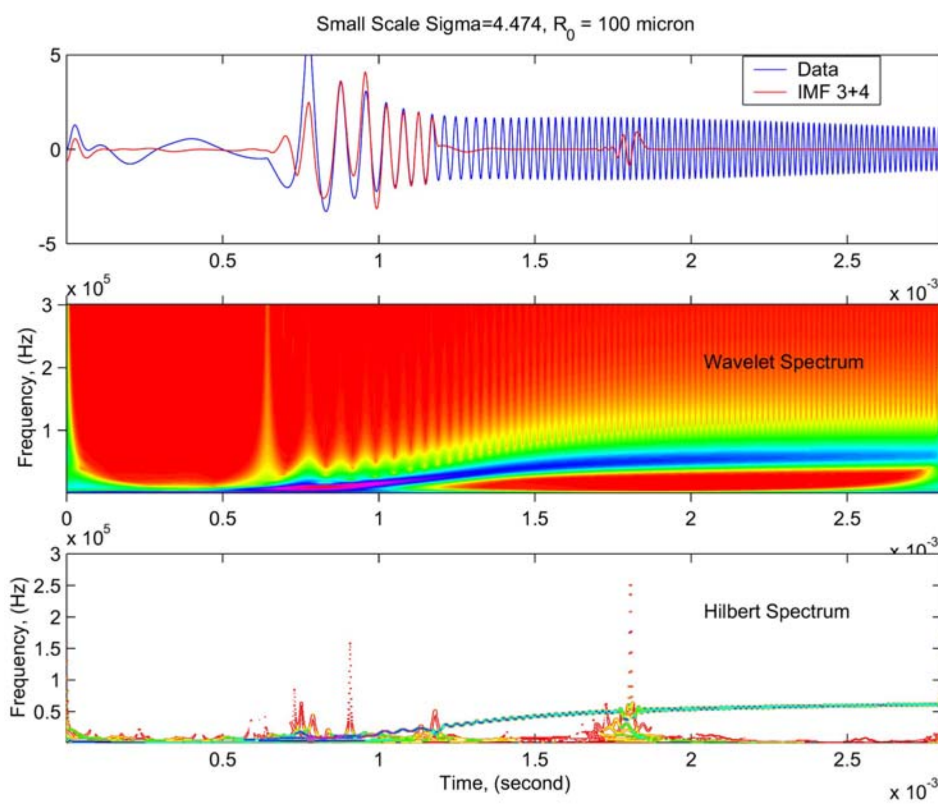

Figure 38. Pressure signal, wavelet and Hilbert transforms for a 100μm bubble in a diffusing vortex

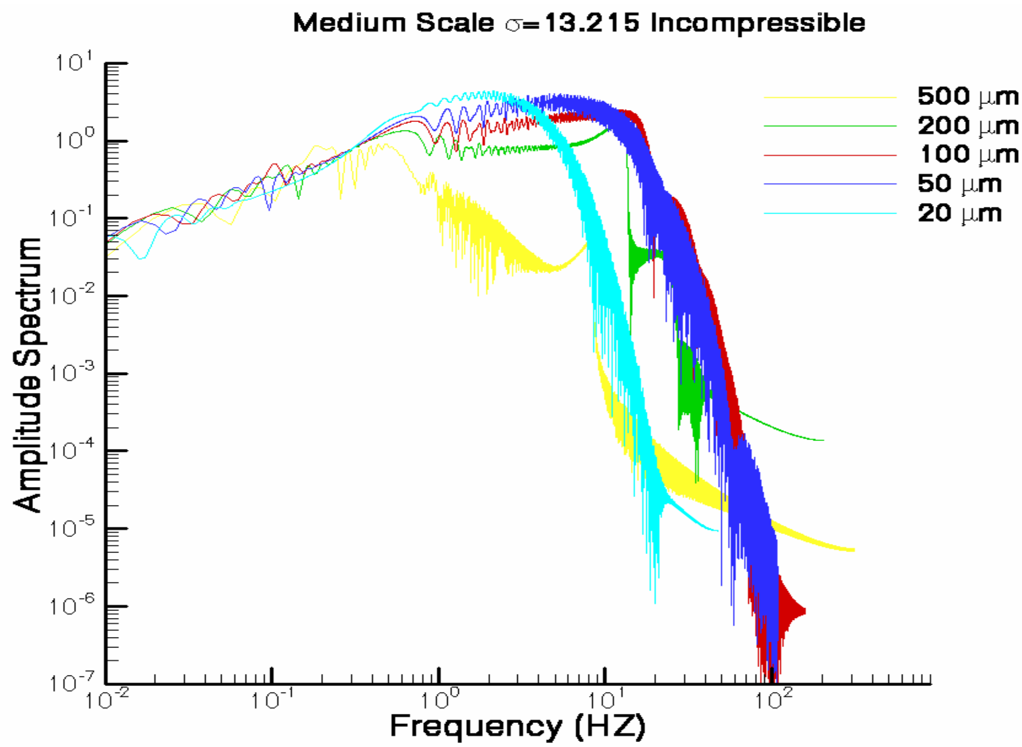

Figure 39. Normalized amplitude spectra for various initial bubble radii in the small-scale tests.

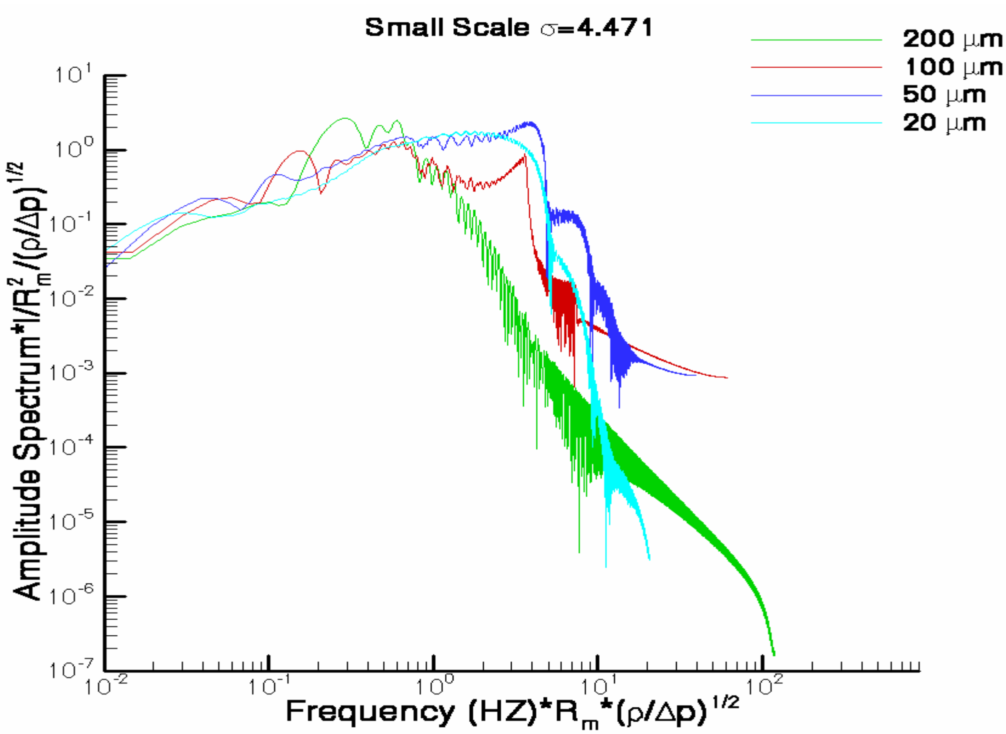

Figure 40. Normalized amplitude spectra for various initial bubble radii in the medium-scale tests.

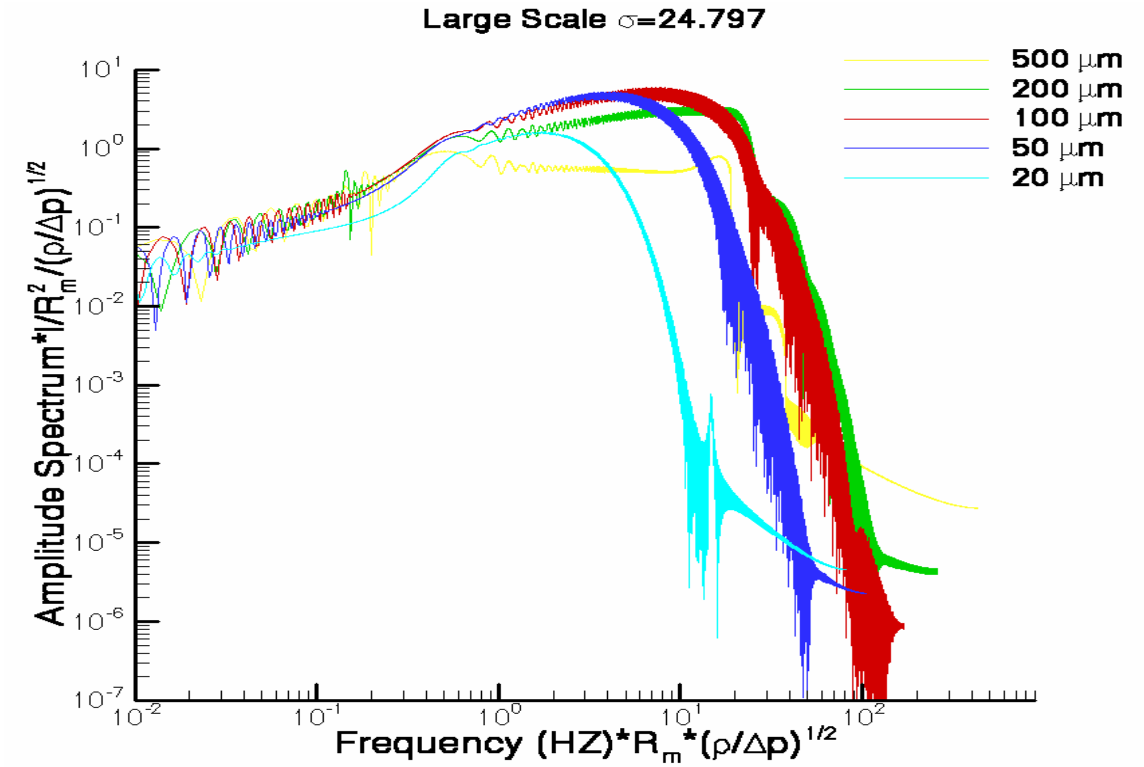

Figure 41. Normalized amplitude spectra for various initial bubble radii in the large-scale tests.

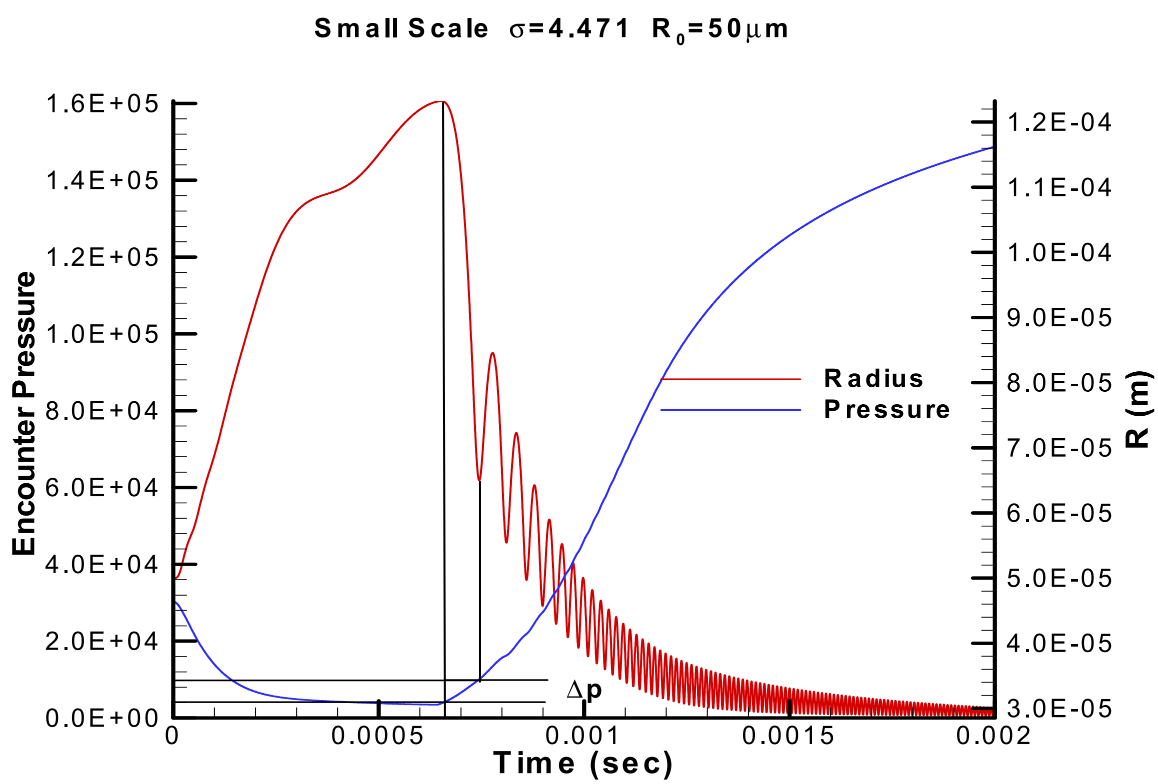

Figure 42. Bubble radius and emitted pressure versus time. Definition sketch of the quantities, R_m and ΔP.

4.6 Effect of Compressibility

An important feature of the problem that should be kept in mind is that the spherical configuration of the bubble surface is unstable during the collapse, so that the analysis based on the assumption of spherical symmetry cannot be rigorously correct. Furthermore, the neglect of liquid compressibility and thermal damping effects, which become important in the subsequent collapses.

All the results presented above were obtained by using the incompressible Rayleigh-Plesset equation. Since it is known that compressibility effects are important during the bubble collapse, it is interesting to compare the results obtained by using the compressible equivalent to the Rayleigh-Plesset equation. Comparing Figures 43a and 43b, one can see that the bubble behaves almost the same until after the first collapse. The strength of the subsequent collapses is attenuated significantly when compressibility is taken into account. Figure 44 illustrates these differences in the frequency domain. The normalized curves in the frequency domain for the medium scale are shown in Figure 45. We can see that the normalized bring together all spectra of the same type indicating that the scaling chosen is adequate.

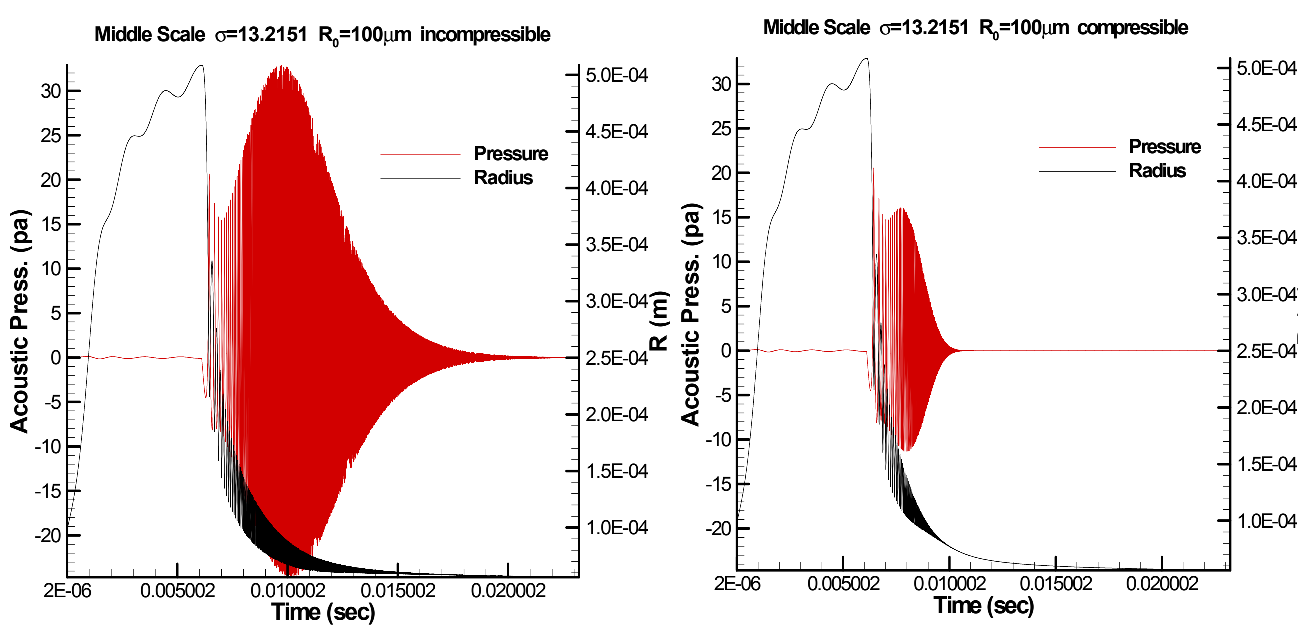

Figure 43. Comparison of the bubble radii and the acoustic pressures versus time when compressible effects are taken into account or when they are ignored.

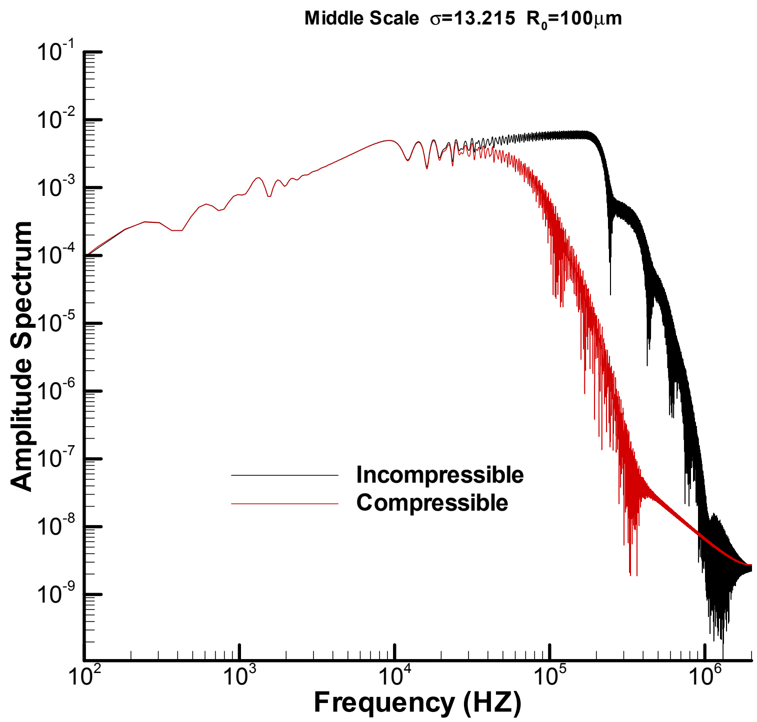

Figure 44. Comparison of the amplitude spectra when compressible effects are taken into account or when they are ignored.

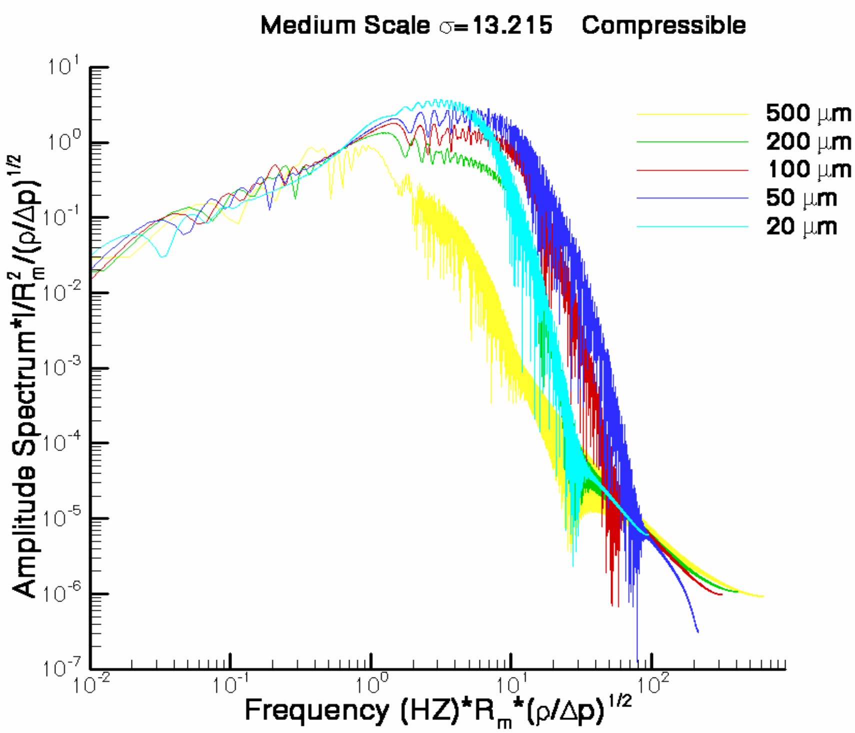

Figure 45. Normalized frequency spectra for different initial nuclei sizes when compressible effects are taken into account.

4.7 Effect of Turbulent Fluctuations

It is know that the tip vortex in the near field where the cavitation inception occurs is highly unsteady due to turbulent fluctuations (Green and Acosta 1991). Lacking unsteady information in the tip vortex core usually leads to under-predicting the cavitation inception number because the turbulent fluctuations are expected to amplify bubble oscillations during growth and collapse. To consider the effect of turbulent fluctuations, artificial sinusoidal fluctuations are added to the original circulation Γ_0 such that

$$\Gamma(t) = \Gamma_0[1 + \quad \sin(2 \quad t)], \tag{4.8}$$

where α is the amplitude and ω is the fluctuation frequency. Figure 46 shows the pressure that a 50µm bubble encounters during capture with and without the artificial sinusoidal fluctuations (α=0.03, ω=1khz) for σ=4.8 in the small-scale case. It is seen from the Figure 47 that without turbulent fluctuations the bubble grows to only a relatively small size when it reaches the vortex axis. As shown in Figure 48, the maximum bubble size and the amplitude of the acoustic emission are significantly increased when the artificial sinusoid fluctuations are added.

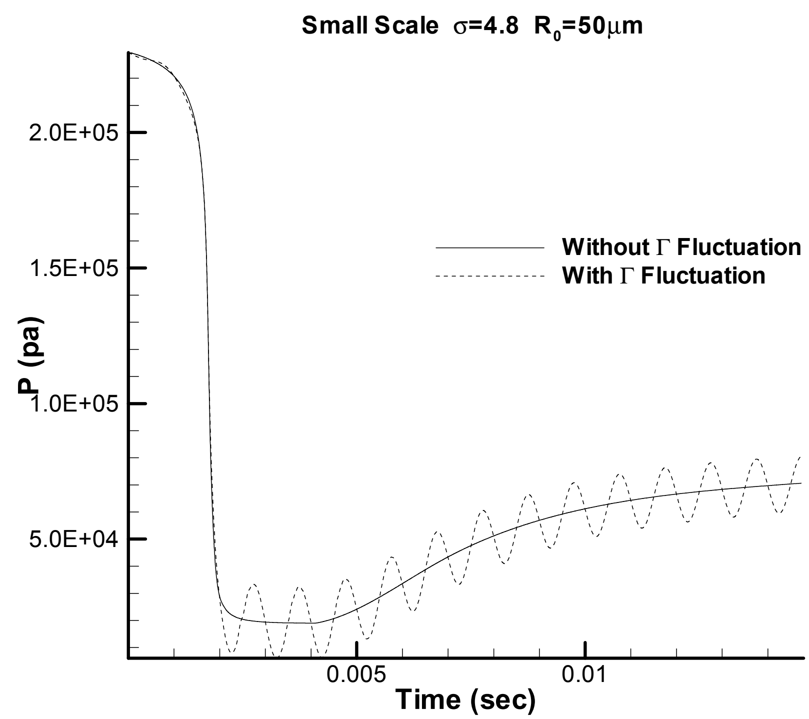

Figure 46. Encounter pressure experienced by the bubble during its capture by the vortex in the presence and in the absence of imposed pressure fluctuations.

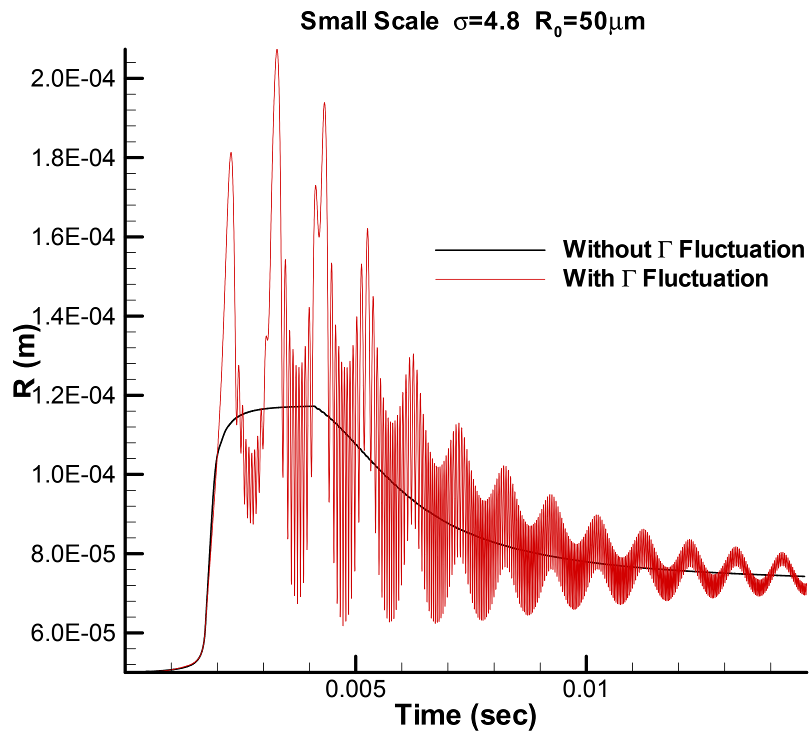

Figure 47. Bubble radius versus time during bubble capture in the vortex in the presence and in the absence of the pressure fluctuations described in Figure 46.

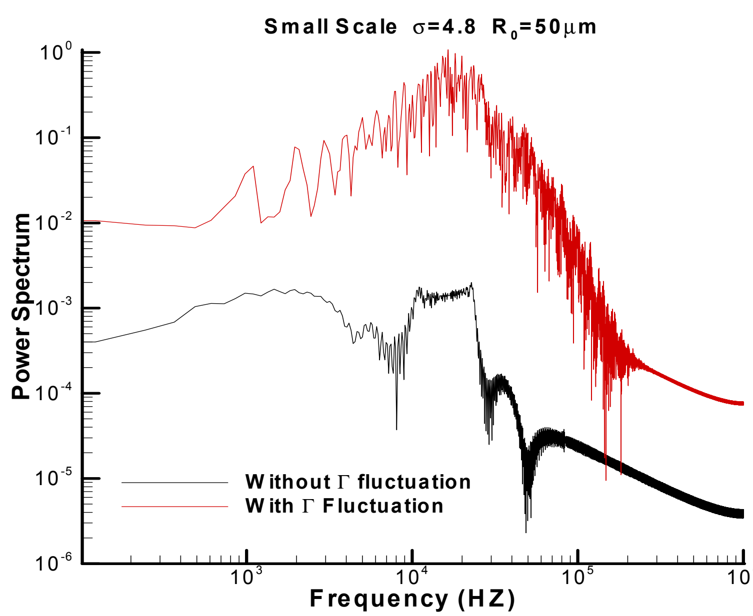

Figure 48. Noise spectra during bubble capture in the vortex in the presence and in the absence of the pressure fluctuations described in Figure 46.

4.8 Effect of Non-Spherical bubble deformation

It was hypothesized in Chahine(1990, 1995) that the non-spherical deformation and bubble breakup contribute to the high frequency noise. To demonstrate the influence of non-spherical deformation, we used the non-spherical model to simulate bubble behavior in the small-scale numerical experiment case. The computations were conducted by releasing bubbles within the vortex core at $0.8a_c$ from the vortex center for both spherical and non-spherical models. The initial gas pressure of the bubble is taken to be the same as at infinity. The bubble deformation was simulated using our non-spherical model, 3DYNAFS™, for R_0 = 50μm in the small-scale conditions and is shown in Figure 49. It is seen that as expected the bubble volume oscillates and changes in time, but also that a re-entering jet is formed on the bubble surface due to the local pressure gradients around the bubble. The computation is terminated when the jet touches the other side of the bubble surface shortly after the bubble first rebound at t = 0.037ms. A comparison between the spherical and the non-spherical bubble models is shown in Figures 50-51. It is seen that bubble volume variations obtained from both models are matched well until the bubble rebound (Figure 50). However, the bubble trajectory predicted by the non-spherical model starts to deviate from the prediction of the spherical model as soon as non-spherical deformations become significant (Figure 51). Of most interest is that high frequency oscillations in the acoustic pressure are observed when the jet touched the other side in the non-spherical model as shown in Figure 52.

Another source of the high frequency noise may come from two parts of the bubble surface colliding. To simulate such an effect a computation was conducted with our axisymmetric version, 2DYNAFS™ , of the non-spherical model, where the bubble with initial radius R_0 = 50μm is released at the vortex center in the small-scale numerical experiment. The initial gas pressure of the bubble is also taken to be the same as at infinity. The bubble contours at various time steps during growth and collapse are shown in Figures 53a and 53b. Figure 53c shows, using the bubble poles and the side node, that the bubble first elongates at the beginning of its growth, then starts to thin at its waist and tends to separate into two. A high frequency acoustic signature is then observed at about t = 0.6ms as shown in Figure 53d when the bubble surfaces collide on the axis. Then the bubble rebounds and re-collapses forming two jet on the axis of rotation, and emits a very strong high frequency sound.

The high frequency acoustic signatures due to non-spherical deformation as shown above are important and may be the major source of cavitation inception noise. This may lead to a significant discrepancy in the prediction of cavitation inception number between the spherical and non-spherical models if an acoustic criterion is used to define the cavitation inception event.

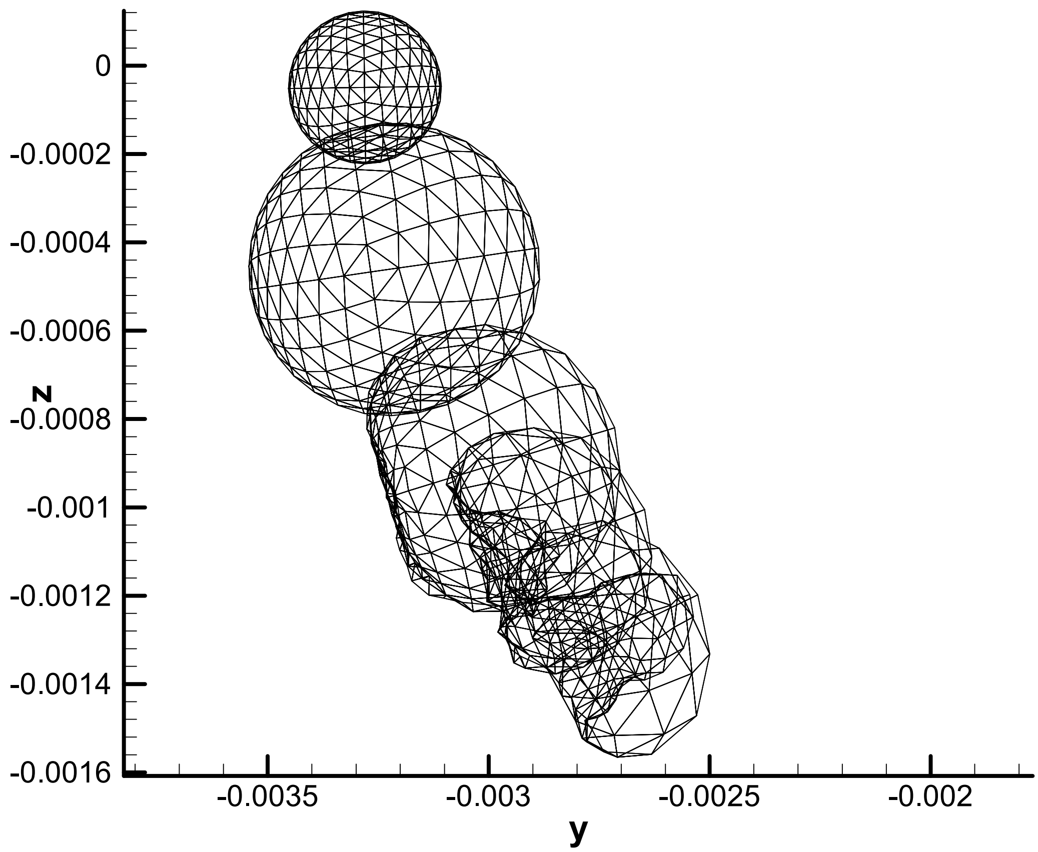

Figure 49. Bubble shape deformation during its capture in the vortex as simulated with 3DYNAFS™.

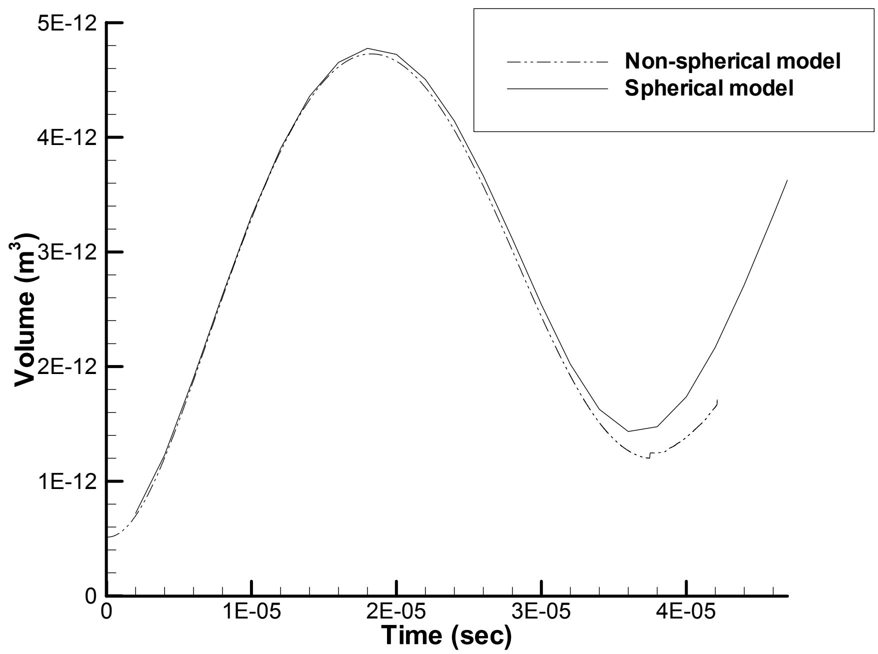

Figure 50. Comparison of bubble volume versus time between spherical and 3D model using 3DYNAFS™.

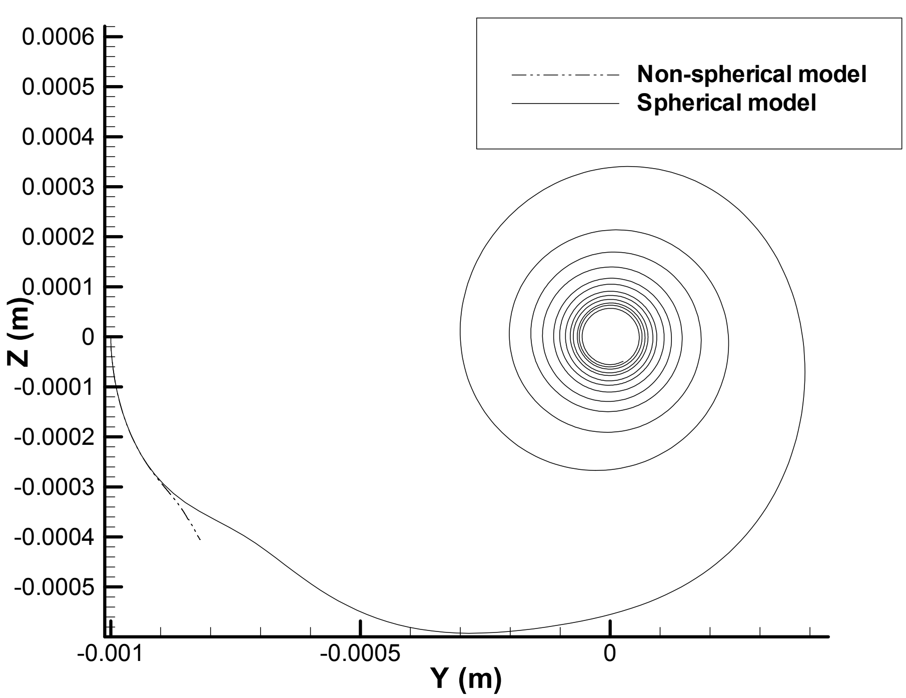

Figure 51. Comparison of bubble trajectory versus time between spherical and 3D model using 3DYNAFS™.

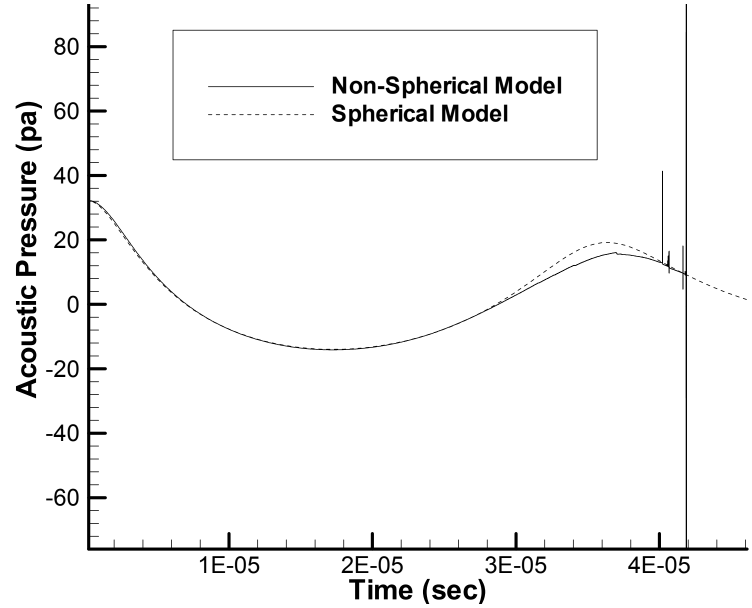

Figure 52. Comparison of acoustic pressure versus time between spherical and 3D model using 3DYNAFS™.

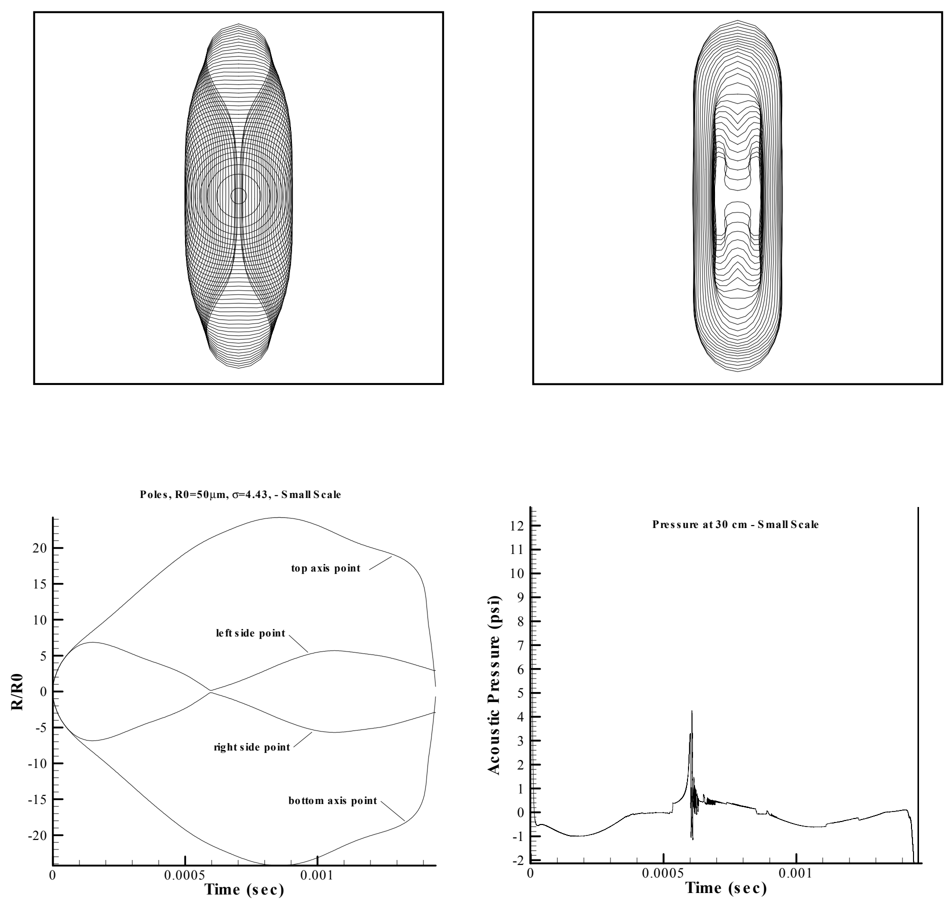

Figure 53. Simulation of bubble dynamics on the vortex axis. a) Bubble growth, elongation and constriction at waist resulting in water-water impact and high pressure spike as shown in d). b) Bubble collapse along axis with two jet formation. c) Pole motion and d) emitted acoustic pressures.

5. CONCLUSIONS

We have applied in this study different bubble dynamics models to predict the cavitation inception of the tip vortex flow. We have shown that using the conventional engineering definition of cavitation inception and the classical spherical model cannot explain the scaling effect due to the nuclei size distribution, which are observed in the experiments. The cavitation inception number predicted by using our “improved” spherical model, however, showed that the nuclei sizes play an important role in scaling the cavitation inception between various scales, especially when the water contained bubbles larger than some critical size depending on the experimental conditions.

We have identified the sources of high frequency acoustic emission: initial bubble growth, and more importantly, subsequent bubble collapse when the bubble reaches the region where the vortex diffuses, and where multiple rebounds and collapses ensue. The adverse pressure gradient and pressure fluctuations along the vortex core were found to significantly increase both the amplitude and frequency of the acoustic emission during bubble capture by the vortex.

We also applied non-spherical bubble dynamics models to demonstrate the importance of the non-spherical deformation on the prediction of cavitation inception. Non-spherical deformations during bubble capture by the line vortex appear to result in high frequency acoustic signatures when the re-entering jet touches the bubble surface. After the bubble enters the vortex center, high frequency acoustic signatures are also observed when liquid-liquid collision occurs during non-spherical deformation along the vortex axis.

6. APPENDIX

6.1 A.1 Derivation of the Modified Rayleigh-Plesset Equation

The velocity potential of an oscillating and moving spherical bubble can be written as the sum of the potential of a source representing the oscillations and a dipole representing the flow about a translating sphere. In the reference frame of the moving bubble with a velocity *U*, we can express ϕ as:

$$\phi = -\frac{R^2\dot{R}}{r} + U\left(r + \frac{1}{2}\frac{R^3}{r^2}\right)\cos\theta\,, \tag{A.1}$$

where U is the relative velocity between the bubble and the liquid (slip velocity). Here we assume the bubble is small so that the background flow can be treated as a uniform flow around the bubble locally. In the absolute reference frame, we have

$$\phi = -\frac{R^2\dot{R}}{r} + \frac{U}{2}\frac{R^3}{r^2}\cos\theta\,. \tag{A.2}$$

The time derivative of the velocity potential is

$$\frac{\partial\phi}{\partial t} = -\frac{2R\dot{R}^2 - R^2\ddot{R}}{r} + \frac{1}{2}\frac{\partial U}{\partial t}\frac{R^3}{r^2}\cos\theta + \frac{3}{2}\frac{R^2\dot{R}}{r^2}U\cos\theta\,, \tag{A.3}$$

and the velocity vector components are given by:

$$u_r = \frac{\partial\phi}{\partial r} = \frac{R^2\dot{R}}{r^2} - U\frac{R^3}{r^3}\cos\theta, \tag{A.4}$$

$$u_\theta = \frac{1}{r}\frac{\partial\phi}{\partial\theta} = -\frac{1}{2}U\frac{R^3}{r^3}\sin\theta. \tag{A.5}$$

At $r = R$ we have

$$\frac{\partial\phi}{\partial t} = -2\dot{R}^2 - R\ddot{R} + \frac{1}{2}\frac{\partial U}{\partial t}R\cos\theta + \frac{3}{2}\dot{R}U\cos\theta\,, \tag{A.6}$$

$$u_r = \dot{R} - U\cos\theta, \tag{A.7}$$

$$u_\theta = -\frac{1}{2}U\sin\theta\,. \tag{A.8}$$

At $r \to \infty$ we have

$$\frac{\partial \phi}{\partial t} = 0, \tag{A.9}$$

$$u_r = 0, \tag{A.10}$$

$$u_\theta = 0. \tag{A.11}$$

From Bernoulli's equation we have

$$\left(\frac{\partial \phi}{\partial t} + \frac{1}{2}|\mathbf{u}|^2 + \frac{P}{\rho} \right)_{r=R} = \left(\frac{\partial \phi}{\partial t} + \frac{1}{2}|\mathbf{u}|^2 + \frac{P}{\rho} \right)_{r \to \infty}, \tag{A.12}$$

$$\begin{aligned} -2\dot{R}^2 - R\ddot{R} + \frac{1}{2}\frac{\partial U}{\partial t} R\cos\theta + \frac{3}{2}\dot{R}U\cos\theta + \frac{1}{2}\dot{R}^2 - U\dot{R}\cos\theta + \frac{1}{2}U^2\cos^2\theta \\ + \frac{1}{8}U^2\sin^2\theta + \frac{P_R}{\rho} = \frac{P_\infty}{\rho}, \end{aligned} \tag{A.13}$$

$$R\ddot{R} + \frac{3}{2}\dot{R}^2 = \left(\frac{1}{2}\frac{\partial U}{\partial t} R + \frac{1}{2}\dot{R}U \right)\cos\theta + \frac{1}{2}U^2 - \frac{3}{8}U^2\sin^2\theta + \frac{P_R - P_\infty}{\rho}. \tag{A.14}$$

Since we assume that the bubble remains spherical, we can obtain an average equation by integrating over the spherical bubble surface. For the terms with $\cos\theta$ we obtain:

$$\begin{aligned} \frac{1}{4\pi R^2}\int_0^\pi \left(\frac{1}{2}\frac{\partial U}{\partial t} R + \frac{1}{2}\dot{R}U \right)\cos\theta \cdot 2\pi R^2 \sin\theta d\theta &= \frac{1}{4}\left(\frac{\partial U}{\partial t} R + \dot{R}U \right)\int_0^\pi \cos\theta\sin\theta d\theta \\ &= -\frac{1}{4}\left(\frac{\partial U}{\partial t} R + \dot{R}U \right)\cos^2\theta \Big|_0^\pi = 0. \end{aligned} \tag{A.15}$$

For the term with $\sin^2\theta$ we obtain:

$$\begin{aligned} \frac{1}{4\pi R^2}\int_0^\pi \left(-\frac{3}{8}U^2\cos\theta \right) \cdot 2\pi R^2 \sin\theta d\theta &= -\frac{3}{16}U^2 \int_0^\pi \sin^3\theta d\theta \\ &= \frac{3}{16}\left(\cos\theta - \frac{1}{3}\cos^3\theta \right)\Big|_0^\pi = -\frac{1}{4}U^2. \end{aligned} \tag{A.16}$$

We finally have the modified Surface Averaged Rayleigh-Plesset equation as

$$R\ddot{R} + \frac{3}{2}\dot{R}^2 = \frac{P_R - P_\infty}{\rho} + \frac{1}{4}U^2. \tag{A.17}$$

6.2 A.2 Fourier Transform

The finite Fourier transformation is defined by

$$P(f,T) = \int_0^T p(t)e^{-i2\pi ft}dt\,, \tag{A.18}$$

where T is the time duration for the finite Fourier transformation, $p(t)$ is the acoustic signal, f is the frequency and $P(f,T)$ is the signal in the frequency domain. It is noted that for the bubble captured by the diffusive vortex core, the acoustic signal is only significant during bubble growth and collapse. After strong collapse the acoustic signal essentially decays to zero. Such acoustic signal can be described as a deterministic transient signal. For the case of a deterministic transient signal $p(t), 0 \le t \le T$, it is common to describe the frequency content of the signal in terms of its Fourier magnitude spectrum $|F_x(f)|$,

$$F_x(f) = \begin{cases} 2P(f,T), & f > 0, \\ P(f,T), & f = 0, \\ 0, & f < 0, \end{cases} . \tag{A.19}$$

Assuming the duration T equals or exceeds the duration of all significant values of the transient, the finite Fourier transform essentially yields sample values of the exact Fourier transform of the transient signal. This follows because the values of the transient outside the time interval of the computation is zero and, hence, all values of the transient are known from minus to plus infinity.

6.3 A.2 Wavelet and Hilbert Transforms

There are a few methods used for processing non-stationary data. Most of them still depend on Fourier analysis - they are limited to linear systems only. The adoption of any such method is almost strictly determined according to the special field in which the application is made.

The spectrogram is the most basic method, which is nothing but a limited time window width Fourier spectral analysis. By successively sliding the window along the time axis, one can get a time-frequency distribution. Since it relies on the traditional Fourier Spectral analysis, one has to assume the data to be piecewise stationary. The wavelet approach is essentially an adjustable window Fourier Spectral analysis. For specific applications, the basic wavelet function can be specified according to its special needs. But, the wavelet form has to be given before the analysis. In most common applications, the Morlet wavelet is defined as Gaussian enveloped sine and cosine wave groups, $\psi(x)=C*\exp(-x^2/2)*\cos(a*x)$. In the commercial MATLAB routine, a equals to 5. In the wavelet analysis used in the present report, a is 5.5, i.e., the cosine wave groups with 5.5 waves. Continuous or discrete, the wavelet analysis is basically a linear analysis. A very appealing feature of the wavelet analysis is that it provides a uniform resolution for all frequency scales. Limited by the size of the basic wavelet function. There are other procedures used to deal with transient data analysis that one can find , for instance in Bendat and Piersol's (1986) book or Cohen's (1995) book on Time-frequency analysis.

Huang, et al (1998), have introduced a general method that requires two steps in analyzing transient signals. The first step is to preprocess the data by the empirical mode decomposition - data is decomposed into a number of intrinsic mode function (IMF) components. The second step is to apply the Hilbert transform to the decomposed IMFs and construct the energy-frequency-time distribution, designated as the Hilbert Spectrum. This procedure provides the instantaneous frequency and energy rather than the global frequency and energy defined by the Fourier spectral analysis. A brief discussion of the procedure follows.

The necessary conditions for us to define a meaningful instantaneous frequency are that the functions are symmetric with respect to the local zero mean and have the same number of zero crossings and extrema. IMF is sought that satisfies two conditions:

(1) in the whole data set, the number of extrema and the number of zero crossings must either equal or differ at most by one; and

(2) at any point, the mean value of the envelop defined by the local maxima and envelope defined by the local minima is zero.

With this definition, the IMF in each cycle, defined by the zero crossing, involves only one mode of oscillation, no complex riding waves are allowed. An IMF is not restricted to a narrow band signal and it can be both amplitude and frequency modulated. In fact, it can be non-stationary.

Therefore, the decomposition is based on the assumptions:

(1) the signal has at least two extrema - one maximum and one minimum;

(2) the characteristic time scale is defined by the time lapse between the extrema; and

(3) if the data were totally devoid of extrema but contained only inflection points, then it can be differentiated once or more times to reveal the extrema.

The essence of the method is to identify the intrinsic oscillatory modes by their characteristic time scale in the data empirically, and then decompose the data accordingly. Contrary to other methods, this method is intuitive, direct, a posteriori and adaptive, with the basis of the decomposition based on and derived from the data.

Having obtained the intrinsic mode function components, we will have no difficulties in applying the Hilbert transform to each component and computing instantaneous frequencies. After performing the Hilbert transform on each IMF component, we can express the data in the following form:

$$X(t) = \sum_{j=1}^{n} a_j(t) \exp(i \int w_j(t) dt) \qquad \text{(A.20)}$$

This equation gives both amplitude and frequency of each component as function of time. The same data if expanded in Fourier representation would be

$$X(t) = \sum_{j=1}^{\infty} a_j \exp(i w_j t) \qquad \text{(A.21)}$$

with both a_j and ω_j constants.

The contrast between these two equations is that the IMF represents a generalized Fourier expansion. The variable amplitude and the instantaneous frequency have not only greatly improved the efficiency of the expansion, but also enabled the expansion to accommodate non-stationary data such as the collapse of a bubble in a given flow field.

7. REFERENCES

Abbott I.H., Doenhoff, A.E. 1959, "Theory of Wing Sections,"

Arndt, R.E., Keller, A.P., 1992, "Water Quality Effects on Cavitation Inception in a Trailing Vortex," *ASME Journal of Fluid Engineering*, Vol. 114, pp. 430-438.

Arndt, R.E and Maines, "Nucleation and Bubble Dynamics in Vortex Flows," *ASME Journal of Fluids Engineering*, Vol. 122, pp. 488-493, 2000.

Basset, A.B., 1888, "A Treatise on Hydrodynamics," Vol 2. ch. 5, Deighton, Bell and Co., Cambridge, England.

Bendat, J.S. and Piersol, A.G., 1986, "Random data: Analysis and Measurement Procedures", 2nd Edn. New York: Wiley.

Boussinesq, J., 1903, "Theorie analytique de la chaleur," vol 2, p. 224, Gauthier-Villars, Paris.

Chahine, G.L. and Shen, Y.T., 1986, "Bubble Dynamics and Cavitation Inception in Cavitation Susceptibility Meters," *ASME Journal of Fluids Engineering*, Vol. 108, pp. 444-452.

Chahine, G.L., 1990, "Nonspherical Bubble Dynamics in a Line Vortex," The ASME Cavitation and Multiphase Flow Forum, Toronto, Canada, Vol. 98, pp. 121-126, June 1990.

Chahine, G.L., Delepoule, E., and Hauwert, P,. 1993 "Study of Interaction Between Bubbles and Vortical Structures," Proceeding of the ASME Cavitation and Multiphase Flow Forum, Washington, D.C., Vol. 153, pp. 39-46, 1993.

Chahine, G. L., 1995, "Bubble Interaction with Vortices," Vortex Flow, Chapter 18, Ed. S. Green, Kluwer Academic.

Chahine, G.L., Sarkar, K., and Duraiswami, R., 1997, "Strong Bubble/Flow Interactions and Cavitation Inception," DYNAFLOW, INC. Technical Report 94003-1ONR March 1997.

Chahine, G.L., and Duraiswami, R.,1998, " Interaction Between Cavitating Bubbles and Vortical Structure" , Third International Symposium on Cavitation, April 1998, Grenoble, France.

Cohen, L., 1995, "Time-Frequency Analysis", Englewood Cliffs, NJ: Prentice Hall.

Duraswami and G.L. Chahine, 1992 " Analytical Study of a Gas Bubble in the Flow Field of a Line Vortex,"' R. Proceedings, ASME Cavitation and Multiphase Flow Forum, ed. O. Furuya, New York, NY, Vol. 135, pp.69-76, 1992.

Fitzpatrick, N., Strasberg, M., 1958, "Hydrodynamic Sources of Sound," Second Symposium of Naval Hydrodynamics, p201-205.

Fruman, D.H., Dugue, C., Cerrutti, P., 1991, “Tip Vortex Roll-Up and Cavitation,” ASME Cavitation and Mutliphase Flow Forum, FED-Vol. 109, pp.43-48.

Gilmore, F.R. 1952, Calif. Inst. Technol. Eng. Div. Rep. 26-4. Pasadena, C.A.

Gopalan, S., Liu, H.L., and Katz, J., “On the Flow Structure, Tip Leakage Cavitation Inception and Associated Noise,” 23rd Symposium on Naval Hydrodynamics, Sep. 17-22, France, 2000.

Green, S.I., Acosta, A.J., 1991, “Unsteady Flow in Tailing Vortices*,” Journal of Fluid Mechanics,* Vol. 227, 00. 107-134.

Haberman, W.L., Morton, R.K., 1953, “An Experimental Investigation of the Drag and Shape of Air Bubbles Rising in Various Liquids,” DTMB Report 802.

Hsiao, C.-T., Pauley, L.L., 1999, “Study of Tip Vortex Cavitation Inception Using Navier-Stokes Computation and Bubble Dynamics model,” *ASME Journal of Fluid Engineering*, Vol. 121, pp. 198-204.

Huang, N. et al., "The empirical mode decomposition and the Hilbert spectrum for nonlinear and non-stationary time series analysis", Proc. R. Soc. Lond. A (1998) Vol 454, pp 903-995.

Johnson, V.E., Hsieh, T., 1966, “The Influence of the Trajectories of Gas Nuclei on Cavitation Inception,” Sixth Symposium on Naval Hydrodynamics, pp. 163-179.

Latorre, R., 1982, “TVC Noise Envelope - An Approach to Tip Vortex Cavitation Noise Scaling,” *Journal of Ship Research*, Vol. 26, No. 1, pp. 65-75.

LeGuen, A., 1998, “Séparation des effets de turbulence et de battement dans l’analyse par vélocimétrie laser de l’écoulement de tourbillon marginal”, Thèse de Doctorat, Université de Nantes, ED 82-329, France.

Ligneul, P., Latorre, R., 1989, “Study on the Capture and Noise of Spherical Nuclei in the Presence of the Tip Vortex of Hydrofoils and Propellers,” *Acustica*, Vol. 68, pp.1 14.

Maines, B.H., Arndt, R.E., 1993, “Bubble Dynamics of Cavitation Inception in a Wing Tip Vortex,” ASME Cavitation and Mutilphase Flow Forum, FED-Vol. 153, pp. 93-97.

Maxey, M.R., Riley, J.J., 1983, “Equation of Motion for a Small Rigid Sphere in a Nonuniform Flow,” *Phys. Fluids*, Vol. 26, No. 4, pp. 883-889.

McCormick, B.W., 1962, “On Cavitation Produced by a Vortex Trailing from a Lifting Surface,” *ASME Journal of Basic Engineering*, Vol. 84, pp. 369-379.

Morrison, F.A., Stewart, M.B., 1976, "Small Bubble Motion in an Accelerating Liquid," *Journal of Applied Mechanics*, Vol. 43, pp. 399-403.

Oseen, C.W., 1927, "Hydrodynamik," p. 132, Leipzig.

Plesset, M. S., 1948, "Dynamics of Cavitation Bubbles*," Journal of Applied Mechanics*, Vol. 16, pp. 228-231.

Sarkar, K., Duraiswami, R., and Chahine, G.L., 1995, "Three-Dimensional Numerical Simulation of Bubble-Vortical Flow Interaction," ASME Cavitation and Multiphase Flow Forum, Hilton Head, SC, Vol. 210, pp.135-143, August 1995.